Università degli Studi di Padova

Dipartimento di Ingegneria dell'Informazione
Corso di Laurea in Bioingegneria

Dual-Probe Shear Wave Elastography in a Transversely Isotropic Phantom

Laureanda:	*Relatore:*
Gioia Bassan	Prof. Alfredo Ruggeri

Anno Accademico 2015/2016

Abstract

Shear Wave Elastography (SWE) is an ultrasound based technique which is able to measure tissue stiffness through the speed of induced shear waves. Tissue stiffness is often related to pathological conditions and detecting mechanical changes can help the recognition of potential diseases. The clinical use of SWE is limited to isotropic tissue due to the difficulty in assessing a theoretical model for more complex tissue and this project therefore aimed to evaluate the possibility of obtaining a full mechanical characterization of a transversely isotropic (TI) phantom with dual-probe SWE. A TI hydrogel phantom was developed and mechanical tests were performed to verify its anisotropy and determine the elastic moduli in both the perpendicular and longitudinal directions. Shear moduli were estimated using conventional and dual-probe SWE comparing the results to theoretical pure-transverse (PT) and quasi-transverse (QT) wave propagation modes. Both mechanical and SWE tests showed that the phantoms were transversely isotropic ($E_T/E_L \simeq 0.81 \pm 0.1$). Moreover, multiple wave propagation modes calculated with dual-probe SWE showed a good agreement with the theoretical curves and indicated the possibility of measuring all the elasticity constants needed to fully characterize an incompressible, TI tissue with dual-probe SWE.

Keywords: Shear wave elastography, transversely isotropic phantom, dual-probe set-up

Acknowledgements

First and foremost, I would like to thank my supervisors Tim Nordenfur and David Larsson for giving me a valid support, guidance and encouragement during my project. Thanks not only for reading the report several times, giving me accurate feedbacks and providing challenging inputs but also for being optimistic and believe in what I was able to do.

Thanks to Anna Bjällmark and Matilda Larsson for showing interest in my project and be willing to create a positive work environment which made me feel part of the group.

Thanks to Peter Arfert for his technical support. This work would not have been possible without his professional expertise.

Thanks to the kind cooperation of Simon Chatelin who helped me in many occasions during the development of the phantoms.

Finally I would like to thank my family who supported and motivated me during my studies and this year I spent abroad.

Contents

List of Figures

List of Tables

Abbreviations

Abbreviation	**Denotation**
A-mode	Amplitude Mode
ARF	Acoustic Radiation Force
B-mode	Brightness Mode
CT	Computed Tomography
FE	Finite Element
FT	Freeze-Thaw
MRI	Magnetic Resonance Imaging
PT	Pure Transverse
PVA	Poly(vinyl alcohol)
QT	Quasi Transverse
RF	Radio Frequency
RSS	Residual Sum of Squares
SSI	SuperSonic Imaging
SWE	Shear Wave Elastography
SWEI	Shear Wave Elasticity Imaging
TI	Transversely Isotropic
WNLLS	Weighted Non-Linear Least Squares

Symbols

Symbol	**Unit**	**Description**
c	m/s	speed of sound
C_{ijkl}	Pa	Stiffness tensor
δ_{ij}	-	Kronecker delta
ε	-	engineering strain
e	-	fractional volume change
E	Pa	Young's modulus
G	Pa	Linear elastic shear modulus
γ	-	shear strain
I	W/m^2	Intensity of the beam
l	m	length
K	Pa	Bulk modulus
λ	Pa	First Lamé constant
μ	Pa	Second Lamé constant (equal to Elastic shear modulus)
ρ	Kg/m^3	Density
σ	Pa	Stress
S_{ijkl}	Pa^{-1}	Compliance tensor
T	-	Strain matrix
u	m	Wave displacement vector
ν	-	Poisson's ratio
v_S	m/s	Shear wave velocity
τ	Pa	Shear stress
z	Pa s/m^3	Acoustic Impedance

Chapter 1

Introduction

In the past centuries, physicians have used palpation as the gold standard procedure for detecting potential diseases in large isotropic tissue. For nodules and tumours, for instance, the emission of fluids from the vascular system into the extra and intracellular space or the loss of lymphatic system cause an increase of local stiffness [12]. Common medical imaging techniques like B-mode ultrasound, Computed Tomography (CT) or Magnetic Resonance Imaging (MRI) are not able to recognise potential diseases when changes in tissue stiffness occur without corresponding changes that are detectable with these techniques.

In 1998, Sarvazyan et al. [5] were among the first to introduce Shear Wave Elasticity Imaging (SWEI) as a support for ultrasound imaging. An acoustic radiation force is generated by an ultrasound transducer and induces low-frequency shear waves propagating through the tissue. Tracking the propagation velocity of this waves, SWEI can obtain an estimation of the local stiffness and add new information to the conventional B-mode image. In 2004, Bercoff et al. [6] introduced a new acquisition method which increases the quality of the image by sending pushes focused at different depths. These techniques have been clinically used only for isotropic tissue such as breast or liver while the studies on anisotropic tissue so far have been on a research basis because of their theoretical difficulties. In fact, shear wave propagation in anisotropic tissue is more complicated because their mechanical behaviour depends on the direction in which the force (i.e. the focused beam) is applied.

At the School of Technology and Health at the Royal Institute of Technology (KTH) in Stockholm, a research group developed a SWE system focusing on isotropic tissue as well as arteries and in particular on the identification and characterization of plaque aggregates in the carotid artery. The following work aims to extend SWE to transversely isotropic (TI) tissue and contribute to the general knowledge of SWE in non-isotropic tissue which could aid in the detection of pathological developments in such tissue. The study includes the development of tissue-mimicking TI phantoms, the assessment of their elastic properties through mechanical and SWE tests and eventually the evaluation of multiple shear wave propagation modes in the developed phantoms.

Chapter 2

Purpose of Study

The purpose of this study was the analysis of multiple wave propagation modes with dual-probe Shear Wave Elastography in order to obtain a full characterization of transversely isotropic tissue and extend SWE to tissue like muscle and tendon. To achieve this purpose, the study was divided into two main parts.

The first part was oriented towards the development of a tissue-mimicking transversely isotropic phantom. Mechanical and SWE tests were to be performed in order to characterize its elastic properties and evaluate SWE as a tool for measuring these parameters in this kind of tissue.

The second part aimed to track shear wave displacement perpendicular to the pushing beam and measure shear wave propagation velocities in different directions. A dual-probe set-up was to be designed and tested on the developed phantoms comparing the results with previous studies. Eventually, the possibility of extend dual-probe SWE to TI tissue was to be evaluated.

Chapter 3

Background

The following section provides the status quo of the work field and leads the reader to understand all the steps that are discussed in the following chapters. In particular, this section has been divided in two main parts. Mechanical properties of tissue are presented through definitions of elastic parameters needed to characterize biological tissue. Isotropic and transversely isotropic cases are discussed in order to understand the difference between them. Once understood the kind of information needed to fully characterize the mechanical behaviour of a tissue, shear wave elastography (SWE) is presented as a technique which is able to give a quantitative evaluation of these parameters. In particular, we will go through ultrasound fundamentals continuing with SWE and the relations between shear wave propagation speed and elastic parameters.

3.1 Mechanical properties of biological tissue

When a force is applied to an object, it induces a deformation resulting in changes of size and shape. Internal forces act to resist this deformation and, as a consequence, the object will reach a final shape when the external forces are removed. When an object is able to come back to its initial shape, it is called elastic [1]. The ratio between the force F and the area A where this force is applied is called stress (σ) and is measured in Pascal (Pa) (Equation 3.1).

$$\sigma = \frac{F}{A} \tag{3.1}$$

As shown in Figure 3.1, a stress σ_{ij} is defined as acting on the i-plane in the j-direction. Normal stress is represented by the components of the stress tensor directed perpendicular to a face (e.g. σ_{11}); along that face, it is called tensile stress if the component is directed outward and compressive stress otherwise. On the other hand, the stress component parallel to a face is called shear stress (e.g. σ_{23}).

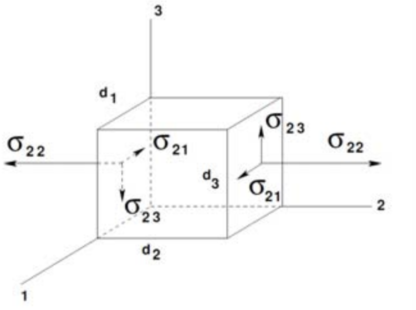

Figure 3.1: Stress components acting on an object. Normal stress is represented by σ_{22} and shear stress is represented by σ_{23} and σ_{21} (adapted from [1]).

The deformation occurring when an object is subjected to a force is measured in terms of strain (ε) which is the relative change of an object dimension. The normal strain in the x_i-direction (with $i = 1, 2, 3$) is:

$$\varepsilon_i = \frac{\partial u_{x_i}}{\partial x} \tag{3.2}$$

where u_{x_i} is the displacement vector along the x_i-direction [2]. Considering the plane (x_i, x_j), the shear strain (γ_{ij}) describes the deformation considering changes of angles in the object. Likewise it can be expressed in terms of the displacement vector as:

$$\gamma_{ij} = \frac{\partial u_{x_i}}{\partial x_j} + \frac{\partial u_{x_j}}{\partial x_i} \tag{3.3}$$

In terms of strain components, $\gamma_{ij} = 2\varepsilon_{ij}$. The knowledge of all ε_{ij} (for $i, j = 1, 2, 3$) enables to express the strain matrix $\mathbf{T}$ and characterize the deformation of the object in every direction [2]:

$$\mathbf{T} = \begin{bmatrix} \varepsilon_{11} & \varepsilon_{12} & \varepsilon_{13} \\ \varepsilon_{21} & \varepsilon_{22} & \varepsilon_{23} \\ \varepsilon_{31} & \varepsilon_{32} & \varepsilon_{33} \end{bmatrix} \tag{3.4}$$

In this thesis we assumed the material being elastic and homogeneous; thus, the mechanical properties are described only by elastic parameters (leaving aside viscous and plastic ones) and do not depend on the position in the body [2]. For small stresses, most materials can be considered linear elastic and have a linear relation between stress and strain. This relation is expressed by Hooke's law and its general form using index multiplication notation is:

$$\sigma_{ij} = C_{ijkl}\varepsilon_{kl} \tag{3.5}$$

where C_{ijkl} is the fourth-order stiffness tensor and consists of the elastic constants [13]. Equation 3.5 can also be written as:

$$\varepsilon_{kl} = S_{ijkl}\sigma_{ij} \tag{3.6}$$

where S_{ijkl} is the compliance tensor which is the inverse of the stiffness tensor [13].

Mechanical properties of biological tissue are described by the stiffness tensor or the compliance tensor. Using Voigt's notation, they are represented by a 6 x 6 symmetric matrix with a number of independent constants varying from 2 to 21 depending on tissue symmetries. At first sight, the number of unknown parameters is 36 but not all of them are required to describe an anisotropic material. Both the stiffness and the compliance matrices are symmetric and have 21 independent parameters in the fully anisotropic case [2]. The matrix formulation of Hooke's law (Equation 3.5) for a generic elastic homogeneous material is [2]:

$$\begin{bmatrix} \sigma_1 \\ \sigma_2 \\ \sigma_3 \\ \tau_{12} \\ \tau_{13} \\ \tau_{23} \end{bmatrix} = \begin{bmatrix} c_{11} & c_{12} & c_{13} & c_{14} & c_{15} & c_{16} \\ c_{21} & c_{22} & c_{23} & c_{24} & c_{25} & c_{26} \\ c_{31} & c_{32} & c_{33} & c_{34} & c_{35} & c_{36} \\ c_{41} & c_{42} & c_{43} & c_{44} & c_{45} & c_{46} \\ c_{51} & c_{52} & c_{53} & c_{54} & c_{55} & c_{56} \\ c_{61} & c_{62} & c_{63} & c_{64} & c_{65} & c_{66} \end{bmatrix} \begin{bmatrix} \varepsilon_1 \\ \varepsilon_2 \\ \varepsilon_3 \\ \gamma_{12} \\ \gamma_{13} \\ \gamma_{23} \end{bmatrix} \tag{3.7}$$

In mechanics, there are some parameters which describe the mechanical behaviour of a material in relation to different physical quantities. Foe example, they relate force and deformation, deformations in different directions and resistance to compression.

Elasticity in linear elastic materials is most commonly expressed in terms of the elastic modulus E (also called Young's modulus) which relates the normal stress to the resulting strain in the same direction ($i = 1, 2, 3$) [14]:

$$E_i = \frac{\sigma_i}{\varepsilon_i} \tag{3.8}$$

The relation between deformations of an object in different directions is expressed by the Poisson's ratio ν_{ji}. It is defined for a uniaxial stress state and relates the lateral strain (x_j-direction) to the axial strain (x_i-direction) according to [14]:

$$\nu_{ji} = -\frac{\varepsilon_j}{\varepsilon_i} \tag{3.9}$$

Thanks to the high content of water, biological tissue is generally assumed incompressible and has a Poisson's ratio of $\nu = 0.5$ [1].

The ability of a tissue to resist a uniform compression is expressed by the bulk modulus K; it relates with both the elastic modulus and the Poisson's ratio according to [14]:

$$K_{ji} = \frac{E}{3(1 - 2\nu_{ji})} \tag{3.10}$$

The ratio between shear stress $\tau_{ij} = \sigma_{ij}$ (with $i \neq j$) and shear strain γ_{ij} is called shear modulus and is denoted by G or μ [14]:

$$\mu_{ij} = \frac{\tau_{ij}}{\gamma_{ij}} \tag{3.11}$$

Table 3.1 presents typical values of the elastic moduli for biological tissues.

Material	E (kPa)
Artery	700-3000
Cartilage	790
Tendon	800
Healthy soft tissues (Breast, kidney, liver, prostate)	0.5-70
Cancer in soft tissues (Breast, kidney, liver, prostate)	20-560

Table 3.1: Typical values of the elastic moduli in biological tissue (adapted from [3]).

3.1.1 Isotropic tissue

A tissue is said to be isotropic if its mechanical properties do not vary with the angular orientation [1]. The general stiffness matrix of Equation 3.7 can be expressed using only two independent parameters, called the Lamé constants, λ and μ.

In such a tissue the Lamé constants are related to the stiffness tensor by:

$$C_{ijkl} = [\lambda \delta_{ij} \delta_{kl} + \mu(\delta_{ik}\delta_{jl} + \delta_{il}\delta_{jk})]\varepsilon_{kl} \tag{3.12}$$

where δ is the Kronecker delta function defined as $\delta_{ij} = 0$ for $i \neq j$ and $\delta_{ij} = 1$ for $i = j$ $(i, j = 1, 2, 3)$.

Therefore, an isotropic tissue can be fully characterized by two parameters, either the two Lamé constants (Equation 3.14) or the elastic modulus and the Poisson's ratio (Equation 3.15). The elastic modulus E is linked to the Lamé constants by:

$$E = \mu \frac{3\lambda + 2\mu}{\lambda + \mu} \tag{3.13}$$

For common biological tissue, λ is approximately 10^5 times larger than μ and Equation 3.13 becomes $E = 3\mu$ [15].

For a linear isotropic elastic tissue, the stiffness matrix (Equation 3.14) and the compliance matrix (Equation 3.15) are obtained from a simplification of the generalized Hooke's law of Equation 3.7 [13].

$$\begin{bmatrix} \sigma_1 \\ \sigma_2 \\ \sigma_3 \\ \tau_{12} \\ \tau_{13} \\ \tau_{23} \end{bmatrix} = \begin{bmatrix} \lambda + 2\mu & \lambda & \lambda & 0 & 0 & 0 \\ \lambda & \lambda + 2\mu & \lambda & 0 & 0 & 0 \\ \lambda & \lambda & \lambda + 2\mu & 0 & 0 & 0 \\ 0 & 0 & 0 & 2\mu & 0 & 0 \\ 0 & 0 & 0 & 0 & 2\mu & 0 \\ 0 & 0 & 0 & 0 & 0 & 2\mu \end{bmatrix} \begin{bmatrix} \varepsilon_1 \\ \varepsilon_2 \\ \varepsilon_3 \\ \gamma_{12} \\ \gamma_{13} \\ \gamma_{23} \end{bmatrix} \tag{3.14}$$

$$\begin{bmatrix} \varepsilon_1 \\ \varepsilon_2 \\ \varepsilon_3 \\ \gamma_{12} \\ \gamma_{13} \\ \gamma_{23} \end{bmatrix} = \begin{bmatrix} 1/E & -\nu/E & -\nu/E & 0 & 0 & 0 \\ -\nu/E & 1/E & -\nu/E & 0 & 0 & 0 \\ -\nu/E & -\nu/E & 1/E & 0 & 0 & 0 \\ 0 & 0 & 0 & 1/\mu & 0 & 0 \\ 0 & 0 & 0 & 0 & 1/\mu & 0 \\ 0 & 0 & 0 & 0 & 0 & 1/\mu \end{bmatrix} \begin{bmatrix} \sigma_1 \\ \sigma_2 \\ \sigma_3 \\ \tau_{12} \\ \tau_{13} \\ \tau_{23} \end{bmatrix} \tag{3.15}$$

3.1.2 Transversely isotropic tissue

A tissue is said to be anisotropic if its mechanical properties vary with the angular orientation. Anisotropy can occur when the tissue has a structural orientation [16]. The most simple anisotropic model is the transverse isotropy. A transversely isotropic (TI) tissue is characterized by a plane of isotropy (x_1,x_2) and an axis of rotational symmetry (x_3) which is perpendicular to the isotropic plane. Every plane containing the axis of symmetry and every plane parallel to the plane of isotropy are planes of symmetry [1].

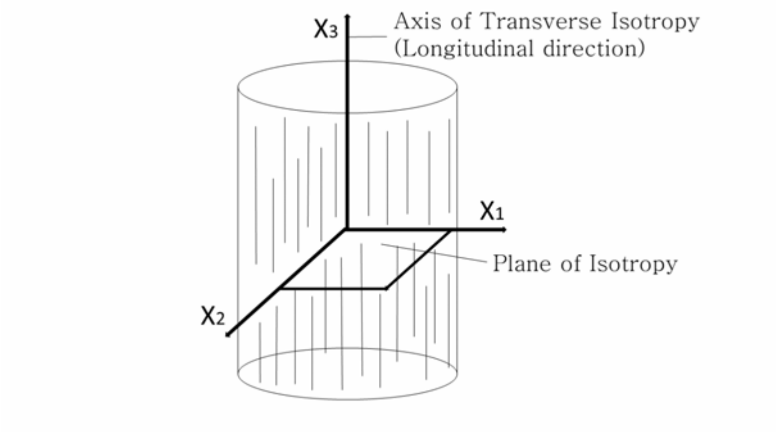

FIGURE 3.2: Schematic representation of a transversely isotropic tissue

The mechanical behaviour of a transversely isotropic tissue is described by five independent elastic constants: c_{11}, c_{33}, c_{66}, c_{44} and c_{13} for the stiffness matrix and E_T, E_L, μ_L, ν_{LT} or ν_{TT} for the compliance matrix [15]. In particular:

- E_T: Elastic modulus in the transverse direction (x_1,x_2);
- E_L: Elastic modulus in the longitudinal direction (x_3);
- μ_T: Shear modulus in the transverse direction (it is not an independent constant and it can be calculated from E_T and ν_{TT} with Equation 3.20);
- μ_L: Shear modulus in the longitudinal direction;
- ν_{TT}: Poisson's ratio in the transverse direction for loading in the perpendicular direction;
- ν_{LT}: Poisson's ratio in the transverse direction for loading in the longitudinal direction.

As in the isotropic case, both the stiffness (Equation 3.16) and the compliance (Equation 3.17) matrices can be simplified to [10]:

$$\mathbf{C} = \begin{bmatrix} c_{11} & c_{11} - 2c_{66} & c_{13} & 0 & 0 & 0 \\ c_{11} - 2c_{66} & c_{11} & c_{13} & 0 & 0 & 0 \\ c_{13} & c_{13} & c_{33} & 0 & 0 & 0 \\ 0 & 0 & 0 & c_{44} & 0 & 0 \\ 0 & 0 & 0 & 0 & c_{44} & 0 \\ 0 & 0 & 0 & 0 & 0 & c_{66} \end{bmatrix} \tag{3.16}$$

$$\mathbf{S} = \mathbf{C}^{-1} = \begin{bmatrix} 1/E_T & -\nu_{TT}/E_T & -\nu_{LT}/E_L & 0 & 0 & 0 \\ -\nu_{TT}/E_T & 1/E_T & -\nu_{LT}/E_L & 0 & 0 & 0 \\ -\nu_{TL}/E_T & -\nu_{TL}/E_T & 1/E_L & 0 & 0 & 0 \\ 0 & 0 & 0 & 1/\mu_L & 0 & 0 \\ 0 & 0 & 0 & 0 & 1/\mu_L & 0 \\ 0 & 0 & 0 & 0 & 0 & 1/\mu_T \end{bmatrix} \tag{3.17}$$

The compliance matrix can be further simplified using Equation 3.18 obtained from the matrix symmetry [10].

$$\frac{\nu_{LT}}{E_L} = \frac{\nu_{TL}}{E_T} \tag{3.18}$$

$$\mathbf{S} = \mathbf{C}^{-1} = \begin{bmatrix} 1/E_T & -\nu_{TT}/E_T & -\nu_{LT}/E_L & 0 & 0 & 0 \\ -\nu_{TT}/E_T & 1/E_T & -\nu_{LT}/E_L & 0 & 0 & 0 \\ -\nu_{LT}/E_L & -\nu_{LT}/E_L & 1/E_L & 0 & 0 & 0 \\ 0 & 0 & 0 & 1/\mu_L & 0 & 0 \\ 0 & 0 & 0 & 0 & 1/\mu_L & 0 \\ 0 & 0 & 0 & 0 & 0 & 1/\mu_T \end{bmatrix} \tag{3.19}$$

While μ_T can be obtained from E_T and ν_{TT} (Equation 3.20), μ_L can only be calculated with shear tests (Equation 3.11) [10].

$$\mu_T = \frac{E_T}{2(1 + \nu_{TT})} \tag{3.20}$$

As shown in Figure 3.3, the elastic modulus of common biological tissue in longitudinal direction is higher than the one in the transverse direction [2].

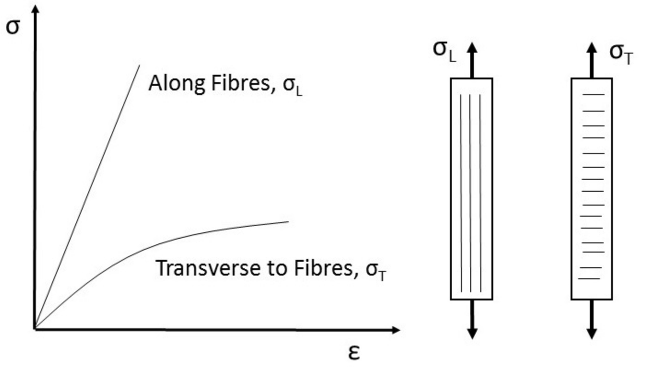

FIGURE 3.3: Stress-strain curves along transverse and longitudinal directions in TI tissue (adapted from [2])

For an incompressible material like biological tissue, the Poisson's ratios can be calculated knowing that the fractional volume change, or dilatation e, of an infinitesimal volume subjected to stresses must be zero [10].

$$e = \frac{1}{E_T}(1 - \nu_T - \nu_L \frac{E_T}{E_L})(\sigma_{11} + \sigma_{22}) + \frac{1}{E_L}(1 - 2\nu_L)\sigma_{33} \tag{3.21}$$

If $e = 0$, the Poisson's ratios satisfy two conditions:

$$\nu_{TT} = 1 - \frac{E_T}{2E_L}, \quad \nu_{LT} = \frac{1}{2} \tag{3.22}$$

Thus, to describe an incompressible TI material three independent elastic constants are needed (E_T, E_L and μ_L), compared to five constants in the general TI case [10].

3.2 Hyperelastic models

Constitutive laws are governing equations relating material stress and strain to one another. In mechanics, hyperelastic constitutive laws are mainly used to model the stress-strain relation of polymeric materials having a rubbery behaviour.

This stress-strain relation is expressed in terms of the strain energy density W, which is the density of the energy stored by a system undergoing deformation [17]. For isotropic solid, W is defined as a function of the three invariants of the strain tensor ($W = W(F) = U(I_1, I_2, I_3)$).

An incompressible material subjected to a uniaxial stress can also be described using principal components of the stresses as:

$$\sigma_i = \lambda_i \frac{\partial W}{\partial \lambda_i} - p \tag{3.23}$$

where p is the unknown hydrostatic stress given by boundary conditions and λ_i are the component of the stretch tensor [18].

The stretch and the stress are defined as:

$$\begin{aligned} \lambda_i = \frac{l_i}{l_{i0}} &= \frac{l_{i0} + \Delta l_i}{l_{i0}} = 1 + \varepsilon_i && (3.24) \\ s_i = \frac{\sigma_i}{\lambda_i} &= \frac{\partial w}{\partial \lambda_i} - \frac{p}{\lambda_i} && (3.25) \end{aligned}$$

where l_i is the final length along the i-direction, l_{i0} the initial length and ε_i the strain.

The principal stretches of an incompressible material undergoing a uniaxial stress are related by the following equation:

$$\prod_{1}^{3} \lambda_i = \lambda_1 \lambda_2 \lambda_3 = 1 \tag{3.26}$$

Considering (x_1, x_2) the plane of isotropy and x_3 the axis of transverse isotropy, we have $\lambda_1 = \lambda_2$ and:

$$\lambda_1 = \lambda_2 = \frac{1}{\sqrt{\lambda_3}} \tag{3.27}$$

3.2.1 Neo-Hookean model

The Neo-Hookean model is a hyperelastic model which is commonly used to approximate the stress-strain curve in rubber-like materials with very limited compressibility [17].

The strain energy density function for an incompressible material is defined as:

$$W = c(I_1 - 3) = (\lambda_1^2 + \lambda_2^2 + \lambda_3^2 - 3) \tag{3.28}$$

where c is a constant related to the material, I_1 is the first invariant of the right Chauchy-Green deformation tensor and λ_i are the principal stretches.

An analytical expression of σ_3 can be obtained applying a uniaxial stress only along the third direction and deriving the strain energy density:

$$\sigma_3 = \lambda_3 \frac{\partial w}{\partial \lambda_3} - \lambda_2 \frac{\partial w}{\partial \lambda_2} = \lambda_3(2c\lambda_3) - \lambda_2(2c\lambda_2) = 2c(\lambda_3^2 - \frac{1}{\lambda_3}) \tag{3.29}$$

The initial elastic modulus E_3, describing the material response at initial loading, is described as:

$$E_3 = \lim_{\lambda_3 \to 1} 2c(1 + \frac{2}{\lambda_3^3}) = 6c \tag{3.30}$$

In uniaxial loading, Equation 3.29 holds in the direction of measurement.

3.2.2 Mooney-Rivlin model

In a Mooney-Rivin solid the strain energy density function W is a linear combination of two invariants of the left Cauchy-Green deformation tensor (I_1, I_2).

$$\begin{aligned} W &= c_1(I_1 - 3) + c_2(I_2 - 3) && (3.31) \\ &= c_1(\lambda_1^2 + \lambda_2^2 + \lambda_3^2 - 3) + c_2(\lambda_1^2\lambda_2^2 + \lambda_2^2\lambda_3^2 + \lambda_1^2\lambda_3^2 - 3) && (3.32) \end{aligned}$$

In the case of uniaxial elongation along the third direction:

$$\sigma_3 = \lambda_3 \frac{\partial W}{\partial \lambda_3} - \lambda_2 \frac{\partial W}{\partial \lambda_2} \tag{3.33}$$

As for the Neo-Hookean model, an analytical expression of σ_3 can be obtained applying a uniaxial stress only along the third direction and deriving the strain energy density.

$$\begin{aligned} \sigma_3 &= \lambda_3(2c_1\lambda_3 + 2c_2(\lambda_3\lambda_2^2 + \lambda_3\lambda_1^2)) + \lambda_2(2c_1\lambda_2 + 2c_2(\lambda_2\lambda_3^2 + \lambda_2\lambda_1^2)) \quad (3.34) \\ &= 2c_1(\lambda_3^2 - \frac{1}{\lambda_3}) - 2c_2(\frac{1}{\lambda_3^2} - \lambda_3) \quad (3.35) \end{aligned}$$

The initial elastic modulus E_3, describing the material response at initial loading, is described as:

$$E_3 = 2c_1(1 + \frac{2}{\lambda_3^3}) - 2c_2(-\frac{3}{\lambda_3^4}) = 6(c_1 + c_2) \tag{3.36}$$

In uniaxial loading, Equation 3.35 holds in the direction of measurement.

3.3 Ultrasound

Ultrasound imaging is a growing medical diagnostic technique used in several applications such as two or three-dimensional imaging of organs, measurement of blood flow motion or evaluation of tissue stiffness. A diagnostic parameter used for the imaging is the acoustic impedance which is a measure of the resistance of the tissue against a given pressure [3]. Differences in acoustic impedance between various biological structures enable ultrasound imaging like the one shown in Figure 3.4.

In diagnostic ultrasound, a piezoelectric transducer encased in a plastic probe produces sound waves converting electrical pulses to mechanical vibrations and then converts the reflected waves into electrical energy to measure their amplitude [19].

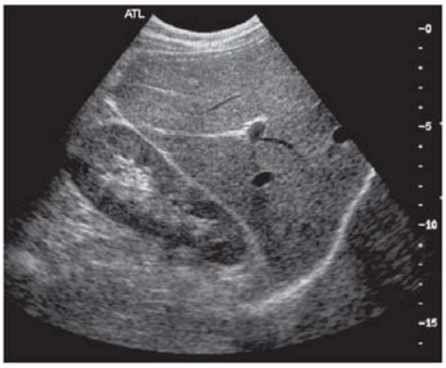

Figure 3.4: An example of B-mode image showing reflections from organs, blood vessel boundaries and scattering tissue (adapted from [3])

A sound wave propagating through tissue generates backwards and forwards oscillations of the particles along its direction of propagation [3]. Clinical applications usually use frequencies between 1 and 18 MHz [20].

When the pulses travel into the body they are reflected and scattered due to variations in acoustical impedance and generate echoes. A two-dimensional image can be obtained by measuring the amplitude of these echoes and considering both the distance from the target to the transducer and the orientation of the ultrasonic beam. The distance is calculated by determining how long it takes the echo to be received from the moment the transducer sent the sound wave with $d = tc/2$ (Figure 3.5), where t is the time, d is the depth and c is the speed of sound in tissue [3]. These echoes travel at an average speed of 1540 m/s in soft biological tissue, 333 m/s in air and 3400 m/s in bones [3].

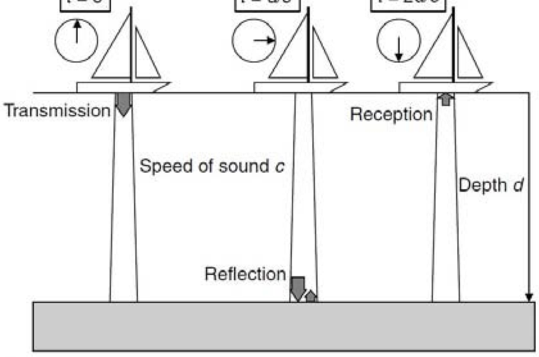

Figure 3.5: Measurement of depth using pulse echo principle (adapted from [3])

There are several modes of ultrasound that are used in medical imaging, for example:

- *A-mode (amplitude mode)*: it is the simplest mode and consists of a single-element transducer sending pulses to scan a single line through the body [21];
- *B-mode (brightness mode)*: an array of transducers simultaneously scans a plane through the body and forms a two-dimensional image [21];
- *M-mode (motion mode)*: it records a video of the structure by sending pulses in quick succession and taking B-mode images over a line each time [3];
- *Doppler mode*: it uses the Doppler effect to measure and visualize moving structures such us blood [3].

When forming a B-mode image, several assumptions are made to simplify the calculations [3]:

- the speed of sound is constant;
- the beam axis is straight;
- the attenuation in a specific tissue is constant;
- the pulse travels only to targets that are on the beam axis and back to the transducer.

3.4 Elastography

Elastography is a medical imaging technique which is able to distinguish tissue by its elastic properties and reveals anatomical structures composed of tissue with different stiffness. Thanks to its ability to obtain quantitative measures, it adds a new quality to conventional imaging techniques such as ultrasound and Magnetic

Resonance Imaging (MRI). Figure 3.6 is an example of ultrasound-based elastography; the pixel intensities represent the values of local shear modulus which is a way to express tissue stiffness. Elastography aims to be a helpful and non-invasive tool for investigating disease condition and replace biopsies which are painful and invasive [16]. Palpation is the common practice to have a qualitative analysis of tissue stiffness and consists of pressing the tissue by hand (mechanical static force) and feeling after stiffer nodules [3]. This method is particularly used to find tumours or nodules in breast and it dates back to 1550 BC in ancient Egypt [16].

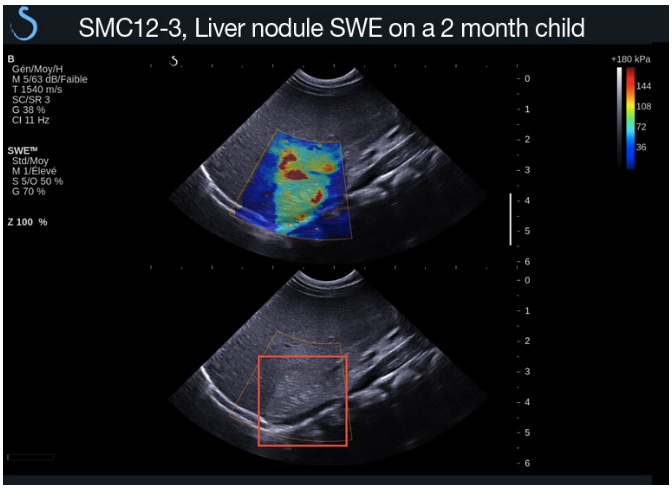

FIGURE 3.6: Liver nodule imaged with an Aixplorer ultrasound system (SuperSonic Imagine, Aix-en-Provence, France)

Ultrasound elastographic techniques can be classified into two main groups according to the measurement principle [3]:

- *Strain technique:* the tissue is compressed and both the tissue deformation and the strain are measured (static method).
- *Shear-wave technique:* shear waves are generated and their velocity within the tissues is measured. From the velocity of propagation it is possible to estimate the shear modulus (dynamic method).

Strain elastography uses an externally applied force induced by a compression and can be done manually by an operator who presses the transducer in and out of the tissue. This technique is not always efficient because of difficulties in reaching deeper tissue and in quantifying the pressure applied [3].

In order to overcome these limitations an acoustic radiation force (ARF) can be used to generate a displacement of the particles in the tissue under consideration [3]. An ARF is induced by the interaction between an acoustic wave and tissue and induces shear waves propagating in the direction perpendicular to the beam. The propagation is caused by a transfer of momentum from the wave to the tissue, arising either from the dissipation or the reflection of the wave [6]. The ARF can be theoretically expressed by:

$$F(\overrightarrow{r},t) = \frac{2\alpha I(\overrightarrow{r},t)}{c} \tag{3.37}$$

where F is the acoustic radiation force, c is the speed of sound in the tissue (typically 1540 m/s), α is the ultrasound attenuation and I the local intensity of the beam. The mechanical displacements in an tissue can be seen as a sum of three contributions using a Green's function:

$$g_{ij}(\overrightarrow{r},t) = g_{ij}^{p}(\overrightarrow{r},t) + g_{ij}^{s}(\overrightarrow{r},t) + g_{ij}^{ps}(\overrightarrow{r},t) \tag{3.38}$$

$g_{ij}^{p}(\overrightarrow{r},t)$, $g_{ij}^{s}(\overrightarrow{r},t)$ and $g_{ij}^{ps}(\overrightarrow{r},t)$ are the three waves that are generated by the ARF and represent the compressional wave (Figure 3.7, top), the low-frequency shear wave (Figure 3.7, bottom) and a coupling term between the previous two waves [6].

The 'pushing beam', or 'pushing pulse', is a focused ultrasonic beam that produces a small movement of the tissue. The displacement produced is typically 1-20 μm, which are sufficient to be detected using an ultrasound system [3].

Different imaging modalities can be used to estimate the resultant tissue displacement and they are selected according to the specific application. Magnetic resonance elastography (MRE) for example is limited to static organs because of its long acquisition time ($\sim$ 20 minutes) [6].

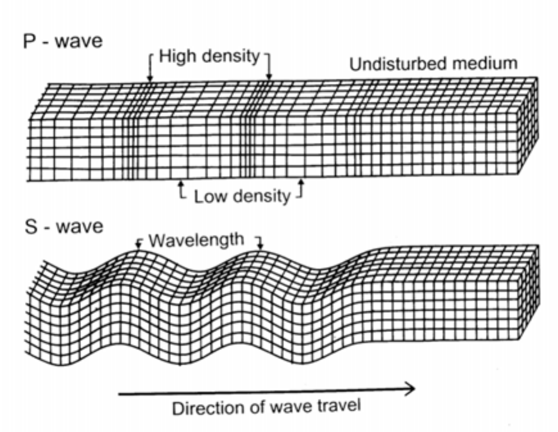

FIGURE 3.7: Compressional wave (P-wave) and shear wave (S-wave) (adapted from [4])

3.4.1 Shear Wave Elastography

Shear Wave Elastography (SWE) is an elastographic technique which relies on the use of shear waves remotely induced by an ARF of a focused ultrasonic beam. This localized ARF is applied to small volumes of tissue (1-8 mm^3) for short duration (less than 1 ms) and the resulting displacements are mapped using ultrasonic correlation-based methods [20]. Shear waves are produced by the vibration of tissue when reached by the pushing beam and travel at a speed v_S. In isotropic, incompressible and linear elastic tissue, the velocity depends on the local density and the local shear modulus according to:

$$v_S = \sqrt{\frac{\mu}{\rho}} \tag{3.39}$$

where v_S is the speed of the wave, μ is the shear modulus and ρ is the tissue density.

Due to the high attenuation of shear waves, mechanical oscillations can be induced only in a limited area near the focal point of the focused beam [5]. In soft tissue, shear wave propagation velocity measured using the ultrasound system is approximately 1-10 m/s [15]. In an isotropic, elastic and incompressible tissue the elastic modulus can be deduced from the shear modulus (Equation 3.13) and the shear wave propagation velocity by :

$$E = 3\mu = 3\rho v_S^2 \tag{3.40}$$

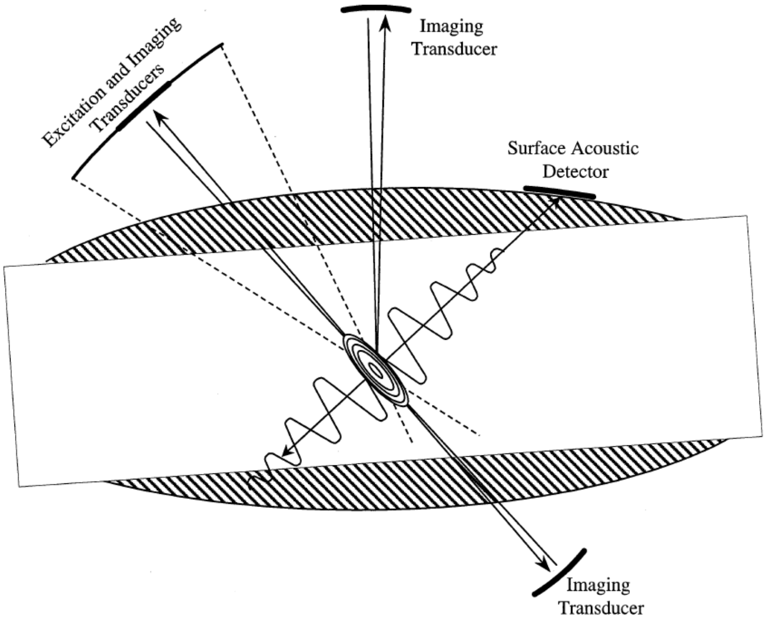

FIGURE 3.8: Schematic representation of shear wave elasticity imaging. A shear wave excitation transducer as well as various imaging transducers and detection sensors are shown (adapted from [5])

Figure 3.8 shows the schematic diagram of shear wave elastography; an excitation focused transducer (ultrasonic phased array or a single focused transducer) generates remote shear waves which propagate through the tissue and are detected by the same or another transducer [5].

Another way of sending the pushing beam is focusing this beam at different depths. It generates shear sources which move faster than the shear waves and create quasi-plane shear waves of stronger amplitude (Figure 3.9) [6]. All the resulting shear waves interfere constructively to create two shear wave fronts propagating in opposite directions [6]. The shear modulus is estimated through the shear-waves propagation in a source-free region.

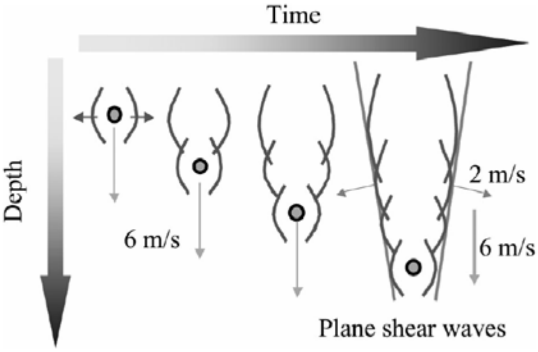

Figure 3.9: Generation of the supersonic shear source introduced by Supersonic Imaging (adapted from [6])

The overall procedure for SWE imaging can be divided in three steps and seen in Figure 3.10. First, an ultrasound transducer sends an ultrasound-focused beam in the tissue at a chosen location. Second, a second transducer, which could also be the same one used for the pushing, starts sending plane-waves insonifications at a high-frame rate in order to catch the shear wave generated by the push and to generate images that will be compared with a reference echographic image acquired before the pushing sequence. Third, the ARF data will be transferred into a computer and processed with cross-correlation algorithms to calculate shear wave propagation velocities [6].

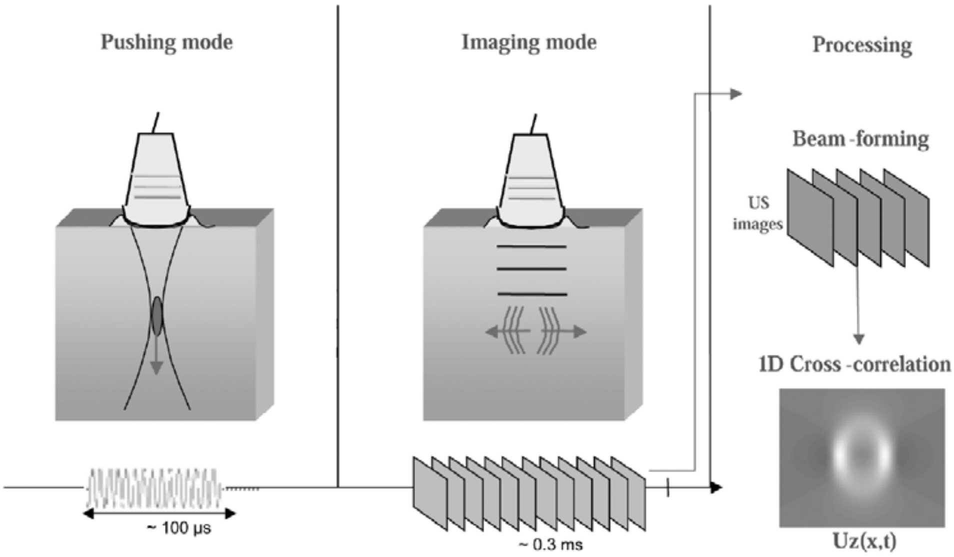

Figure 3.10: Experimental protocol (adapted from [6])

After processing the data with cross-correlation algorithms, shear wave propagation can be seen in the sequenced B-mode images. Figure 3.11 shows a simulation of what B-mode images display.

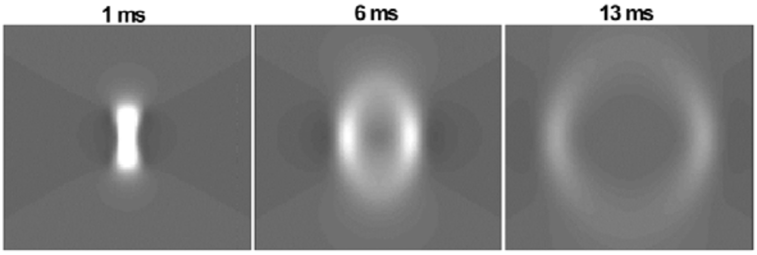

FIGURE 3.11: Simulation of the longitudinal displacements induced by the acoustic radiation force (adapted from [6])

In the past years, Shear Wave Elastography has been a interesting research topic because of its non-invasive evaluation of tissue elastic properties but its clinical use is limited to isotropic tissue like breast [22, 23], prostate [24] and thyroid [25]. However, the strength of SWE lies in the promising results in tissue in which is not possible to perform manual palpation. Many studies were performed to extend SWE to tissue like liver [26, 27], muscle [28], cornea [29] and Achilles tendon [30] and they all show that applicability of SWE could be extended not only to detect tumours in different and more complex tissue but also to detect other pathologies related to tissue stiffness. For example, imaging the cornea using SWE could be used to anticipate and prevent some corneal pathologies like Keratoconus or to evaluate the biomechanical response after a surgery or a treatment [29]. Moreover, SWE could be used to diagnose pathologies related to arterial wall stiffness [31] or to muscles and tendons stiffness [30]. In general, the limit in the use of SWE in these kind of tissue is the difficulty in finding a theoretical model of shear wave propagation for these complex structures.

3.4.2 Shear wave propagation in Transverse Isotropic tissue

The general equation for an anisotropic homogeneous tissue undergoing a force $f_i = (f_1, f_2, f_3)$ is:

$$\rho \frac{\partial^2 u_i}{\partial t^2} - \frac{\partial \sigma_{ij}}{\partial x_j} = f_i \tag{3.41}$$

where $\overrightarrow{u}$ is the displacement, $\partial \sigma_{ij} / \partial x_j$ the stress gradient, t the time and x_i the Cartesian coordinate [32].

In order to give an analytic description of plane wave propagation we assume no external forces and express the acceleration of an infinitesimal volume using Newton's second law as [10]:

$$\frac{\partial \sigma_{ij}}{\partial x_j} = \rho \frac{\partial^2 u_i}{\partial t^2} \tag{3.42}$$

Substituting the Hooke's law of Equation 3.5 in Equation 3.42 we obtain [10]:

$$c_{ijkl} \frac{\partial u_k}{\partial x_j \partial x_i} = \rho \frac{\partial^2 u_i}{\partial t^2} \tag{3.43}$$

In the measurement of shear wave propagation velocity, it is important to understand the difference between phase and group velocity. Sometimes their definition differs when considering different media; phase velocity occurs either due to non-isotropy or due to viscosity and, in this case, different frequencies propagate at different velocities. Consider an observer and a point source radiating plane waves equally in all directions in a non-dispersive medium, as shown in Figure 3.12. The group velocity v_r is calculated by the ratio between the distance from the source to the observer and the transit time between them. It corresponds to the speed of a wave packet along the direction ϕ_r. If either the distance between the source and the observer or the transit time is unknown, a measure of the phase velocity v_ω can be done by observing the wave travel in a small region so that any wave appears to be plane. It corresponds to the speed of a plane wave travelling perpendicularly to the wave front [7].

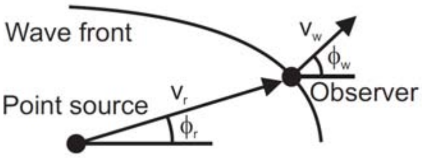

FIGURE 3.12: Phase and group velocity (v_ω and v_r respectively) measurement for a wave emitted from a point source in an anisotropic medium (adapted from [7]).

In a non-dispersive isotropic object, phase and group velocities are identical, while in a non-isotropic object these velocities are generally different along the same direction. In this study we neglected the effect of viscosity and considered only non-dispersive tissue.

Christoffel equation is obtained defining a harmonic (steady-state) plane wave $u_k = U_k e^{k\omega(n_j x_j / v_\omega - t)}$, where **U** is the polarization vector, ω the angular frequency, v_ω the phase velocity and n the unit vector orthogonal to the wave front and substituting it in Equation 3.43 [32]:

$$\begin{bmatrix} G_{11} - \rho v_\omega^2 & G_{12} & G_{13} \\ G_{21} & G_{22} - \rho v_\omega^2 & G_{23} \\ G_{31} & G_{32} & G_{33} - \rho v_\omega^2 \end{bmatrix} \begin{bmatrix} U_1 \\ U_2 \\ U_3 \end{bmatrix} = 0 \tag{3.44}$$

where G_{ik} are the Christoffel matrices which depend on the material properties and the direction of the wave propagation [32]:

$$G_{ik} = c_{ijkl} n_j n_l \tag{3.45}$$

For non-dispersive and TI tissue, the solution of Equation 3.44 corresponding to pure shear wave is:

$$v_\omega^2 = \frac{c_{66} sin^2\phi_\omega + c_{44} cos^2\phi_\omega}{\rho} \tag{3.46}$$

where ϕ_ω is the angle between the direction of the wave propagation and the direction of the fibres in the propagation plane and c_{ij} are the components of the stiffness matrix (Equation 3.16) [33].

The group velocity v_r can be expressed by a transformation of the phase velocity v_ω as:

$$v_r = \sqrt{v_\omega^2 + (\frac{dv_\omega}{d\phi_\omega})^2} \tag{3.47}$$

$$\phi_r = \phi_\omega + arctan(\frac{1}{v_\omega}\frac{dv_\omega}{d\phi_\omega}) \tag{3.48}$$

The theoretical expression for the group velocity is given by [33]:

$$v_r(\phi) = \sqrt{\frac{c_{44}c_{66}}{\rho(c_{44}sin^2(\phi_r) + c_{66}cos^2(\phi_r))}} \tag{3.49}$$

Using shear wave elastography to measure the velocity of shear wave in tissue we can determine the components of the stiffness matrix. First, the constants c_{11} and c_{33} are determined from the measurement of longitudinal ultrasound velocities in direction perpendicular (v_{L1}) and parallel (v_{L3}) to the fibres axis (x_3). Second, the constants c_{44} and c_{66} which are the shear moduli in longitudinal and transverse directions respectively, can be determined from the velocities of the shear waves propagating in direction perpendicular (v_{S1}) and parallel (v_{S3}) to the fibres axis with Equation 3.49 [15]. Third, according to the theory of Levinson [34], c_{13} can be assumed being $c_{13} \simeq \sqrt{c_{11}c_{33}}$ while reducing the number of independent constants and simplifying the resulting equations.

$$c_{11} = \rho v_{L1}^2 \tag{3.50}$$

$$c_{33} = \rho v_{L3}^2 \tag{3.51}$$

$$c_{66} = \rho v_{S1}^2 \tag{3.52}$$

$$c_{44} = \rho v_{S3}^2 \tag{3.53}$$

$$c_{13} \simeq \sqrt{c_{11}c_{33}} \tag{3.54}$$

In soft tissue, the typical values for these parameters are: $\rho \simeq 1100$ Kg/m^3, $c_{11}, c_{33}, c_{13} \sim 3$ GPa, $c_{44}, s_{66} \sim 100$ kPa, and $v_{S1}, v_{S3} \simeq$ 1-10 m/s [15].

Afterwards, the mechanical properties of a tissue can be expressed through its elastic moduli calculating them from the stiffness coefficients. In a transversely isotropic phantom, the two elastic moduli E_T and E_L are related to the stiffness constants according to [15]:

$$E_T = \frac{4c_{66}E_L}{E_L + \gamma c_{66}}, \quad \gamma = \frac{c_{33}}{c_{11} - c_{66}} \tag{3.55}$$

For TI tissue, the perpendicular elastic modulus E_T lies between $3\mu_T$ and $4\mu_T$. These boundaries are given by the value of the E_T in the isotropic case ($E_T = E_L$) and in a tissue having a E_L much larger than E_T ($E_T << E_L$) respectively [15]. This approximation is valid for muscles, for which $E_L \cong 100$ kPa and $c_{44} = \mu_L \leq 10$ kPa, with v_S between 1 and 3 m/s [28].

E_T and E_L can be estimated by [15]:

$$\begin{aligned} E_L &= = \frac{c^2}{c_{11} - c_{66}} && (3.56) \\ E_T &= \frac{4c_{66}c^2}{c^2 + c_{33}c_{66}} && (3.57) \\ c^2 &= c_{33}(c_{11} - c_{66}) - c_{13}^2 && (3.58) \end{aligned}$$

A common approach to validate medical imaging techniques is the use of tissue-mimicking phantoms. Gelatin, hydrogels, agarose and silicon have been used in the past to study isotropic tissue [35] but a transversely isotropic phantom is needed to model the characteristics of biological tissue having a dominant fibers direction such as muscle, tendon or cerebral tissue [36].

Polyvinyl alcohol (PVA) cryo-hydrogel is a polymer of great interest thanks to its ability to absorb a large amount of water; it has mechanical properties which are similar to the ones of biological tissue. The formation of crystallites is obtained by cycles of freezing and thawing in which the sample is repeatedly frozen for approximately 12 hours and thawed back at room temperature for another 12 hours. The strength of the physical crosslinks increases with the number of freeze-thaw (FT) cycles [35].

Qin et al. [37] developed an anisotropic phantom for Magnetic Resonance Elastography (MRE) by embedding Spandex fibres in PVA. Although this method is feasible for MRE, it leads to high acoustic losses between PVA matrix and the Spandex fibres when using ultrasound-based elastography [36]. Millon et al. [38] proposed another method to induce anisotropy in a PVA phantom for cardiovascular applications; stretching the physical crosslinks of the polymeric chains generates a transversely isotropic phantom solving the problem of the acoustic losses. In the same way, Chatelin et al. [36] developed a TI phantom adapting the procedure described by Millon to large tissue which became the starting point for this project.

Chapter 4

Methods

The study was divided in four phases:

1. development of a transversely isotropic phantom;
2. assessment of transverse isotropy through mechanical tests;
3. assessment of transverse isotropy through conventional Shear Wave Elastography;
4. measurement of the mechanical properties of the phantom using dual-probe shear wave elastography.

4.1 Phantom Construction

The phantom was made of poly(vinyl alcohol) (PVA) cryogel to mimic the mechanical properties of biological tissue. The transverse isotropy was achieved by stretching the physical crosslinks of the polymeric chains during repeated freeze-thaw cycles [36]. The samples were prepared diluting a 7 wt% fully hydrolyzed PVA (molecular weight: 56.140 g/mol, density: 1.269 g/cm^3, Sigma-Aldrich, St. Louis, MO) solution in 90 wt% deionized water and 3 wt% of graphite powder (molecular weight: 12.01 g/mol, density: 5 gr/cm^3, particle size $\leq 50\mu$m, Merck

KGaA, Darmstadt, Germany) was added as scattering for the ultrasound measurements. The solution was poured in a 160×50×60 mm^3 parallelepiped mold and underwent two freeze-thaw cycles (24h per cycle, the thawing time for each phantom is reported in Table 4.1). After the first two cycles the phantom was removed from the mold and downsized by cutting away the bottom and the top parts to obtain a final height of 35 mm. Afterwards, as shown in Figures 4.1 and 4.2, the remaining part was unidirectionally stretched in order to maintain a constant static strain. In this study the phantom was stretched to 160% of its initial length before proceeding with an additional three FT cycles (see Figure 4.1). After a total of five FT cycles, the sample was removed from the set-up, cut to obtain samples to use for the mechanical tests (25×25×25 mm) and stored in a box filled with water.

When designing the equipment used to stretch the phantom (Figure 4.3) it was important to consider a few aspects. First, the set-up needed to be small enough to be placed into the freezer during the freezing cycles; second, sand paper needed to be glued to the gripping section to avoid that the phantom slipped out of the set-up; third, the gripping section needed to be wide enough to hold the phantom tightly. The final design can be seen in Figure 4.3.

FIGURE 4.1: Picture of the phantom 160 mm long. 30 mm on each side of the phantom were used as a gripping section, the remaining 100 mm were stretched to 160 mm.

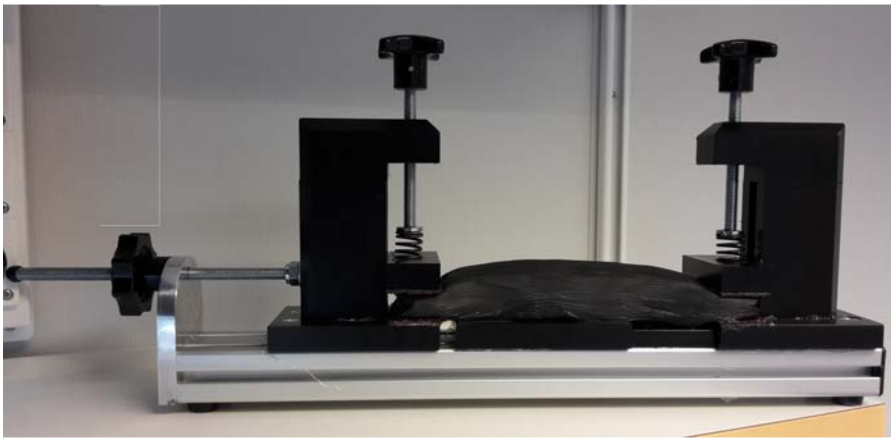

Figure 4.2: Picture of the overall set-up used to stretch the phantom. The right clamp is fixed to the support and the position of the left clamp is controlled through the screw on the left.

Phantom	PVA density	Thawing time
1	7%	12h
2	7%	12h
3	7%	12h
4	7%	14h
5	7%	14h
6	5%	14h
7	5%	14h

Table 4.1: PVA density and thawing time for each phantom.

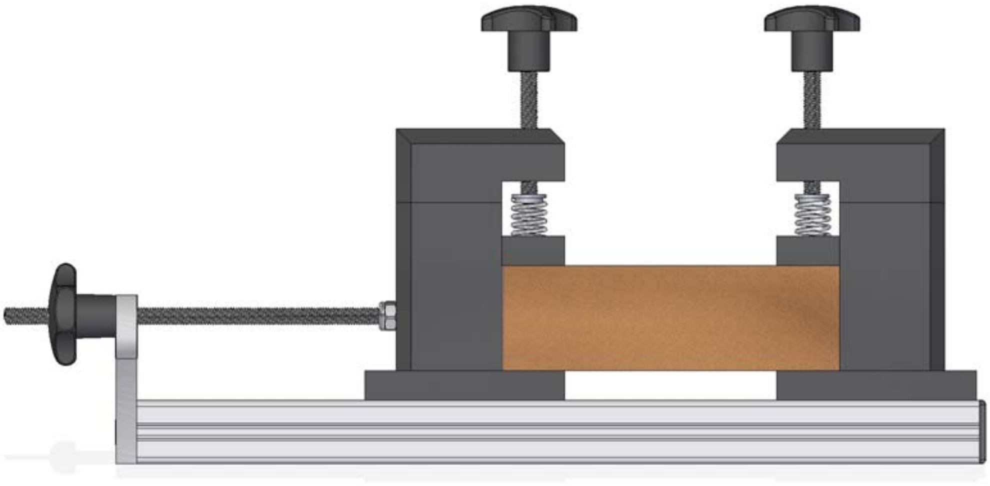

(a)

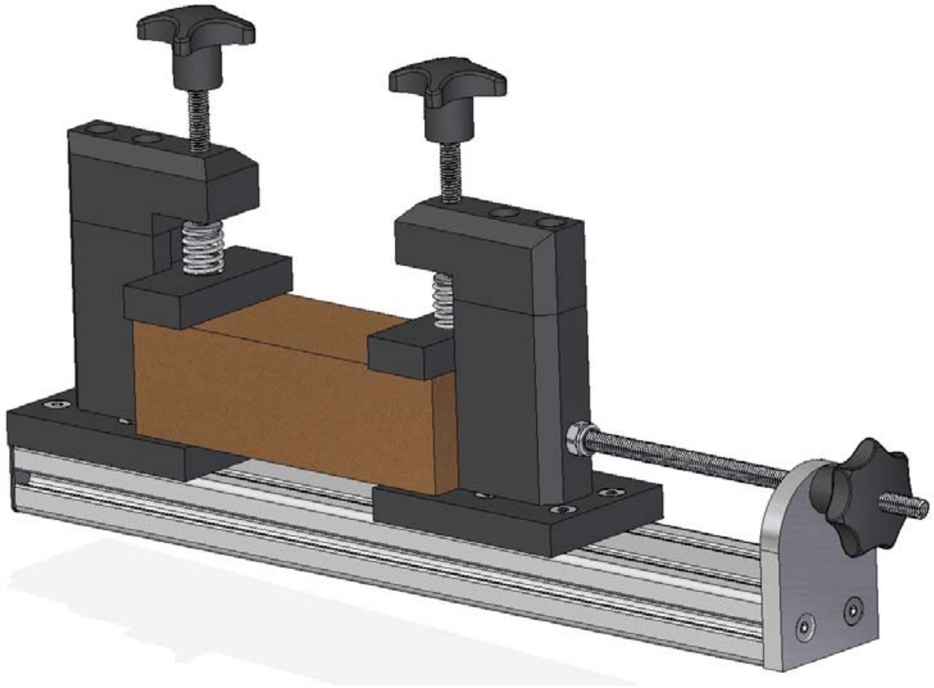

(b)

Figure 4.3: Drawings of the set-up used to stretch the phantom.

4.2 Mechanical tests

The mechanical tests were performed using an Instron 5567 (Instron Worldwide, Norwood, MA, USA) (Figure 4.4) and the process was controlled by a connected computer using Bluehill 2 (Version 2.17 2005, Instron). Each specimen was obtained by cutting a small cube (approximately 25x25x25 mm^3) from the central part of each phantom.

Figure 4.4: Specimen undergoing a compression test with an Instron 5567

Compression tests were performed on the specimens and a pre-compressive load of 2 N was applied to reduce the effects of potential oblique surfaces. During the test, each specimen underwent a constant compression of 5 mm/s for 1.5-2 seconds and the load was measured with the load cells. Dividing the load over the area and the elongation over the length of the specimen we obtained stress-strain curves for each direction. Afterwards, the elastic moduli in longitudinal and transverse direction were calculated as the slope of these stress-strain curves.

An overall of six tests were performed on each specimen, four for the transverse and two for the longitudinal directions. In the transverse direction, the four tests were used to evaluate the assumption of transverse isotropy and were done by applying the same constant compression on the specimen tilting it each time by 90 or 180 degrees (Figure 4.5). The same was done in measuring the elastic modulus in the longitudinal direction (Figure 4.6). The two measurements were obtained tilting the specimen by 180 degrees and applying the same constant compression.

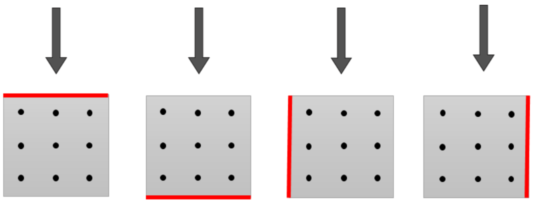

FIGURE 4.5: Mechanical set-up in the plane of isotropy. The red line is used as a reference and represents the top of the phantom.

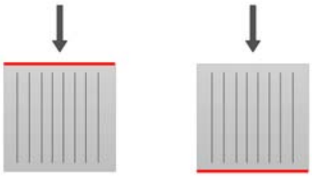

FIGURE 4.6: Mechanical set-up in the longitudinal direction. The red line is used as a reference and represents the right side of the phantom.

4.2.1 Constitutive model fitting

Different post-processing methods were used to fit the stress-strain curve and estimate the elastic modulus between 0% and 5% of the strain. Neo-Hookean and Mooney-Rivlin hyperelastic constitutive models for incompressible materials were compared to linear interpolation (Hooke's law of Equation 3.5) to evaluate if the phantom could be described as a linear elastic or as a non-linear elastic material. For the data processing we used Matlab R2014b (MathWorks, Inc., Natick, Massachusetts, United States) and the implementation can be seen in Appendix A. Table 4.2 presents the stress-strain relations in the three different constitutive models explained in the Chapter 3.

Model	Formula	Elastic modulus
Hooke's law	$\sigma = c_1\varepsilon$	$E = c_1$
Neo-Hookean	$\sigma = 2c_1(\lambda^3 - \frac{1}{\lambda^3})$	$E = 6c_1$
Mooney-Rivlin	$\sigma = 2c_1(\lambda^2 - \frac{1}{\lambda}) - 2c_2(\frac{1}{\lambda^2} - \lambda)$	$E = 6(c_1 + c_2)$

TABLE 4.2: Stress-strain relations used by the constitutive models where σ is the stress, ε the strain, λ the stretch, E the elastic modulus and c_1 and c_2 are the model's constants.

The fitting of the data was done with the Linear Least Square (LLS) method. This algorithmic technique finds the solution which minimizes the sum of the squares of the residuals that are the differences between the data and the estimated curve.

After obtaining the elastic moduli in the two directions, the estimated velocity was calculated. As explained in section 3.4.2, in a transversely isotropic and homogeneous phantom the group velocity along a direction is related to the shear modulus in that direction according to [20].

$$v_S = \sqrt{\frac{\mu}{\rho}} \tag{4.1}$$

In the plane of isotropy the shear modulus μ_T can be calculated using [10]:

$$\mu_T = \frac{E_T}{2(1+\nu_{TT})} \tag{4.2}$$

Assuming isotropy in the longitudinal direction, the shear modulus is:

$$\mu_L = \frac{E_L}{2(1+\nu_{LT})} \tag{4.3}$$

Phantom density was calculated using Archimede's principle on several phantoms. For each of them, a small sample was put in a water-filled cylindrical beaker after having been weighted. The volume of the inserted phantom, V, was measured through the change in water level in the beaker and the density was estimated by:

$$\rho = \frac{m}{V} \tag{4.4}$$

where m is the mass of the sample.

The speed of sound was assumed being 1540 m/s, that is equal to the one of biological tissue.

In order to obtain a quantitative estimation of the difference between constitutive models, a paired t-test was performed on pairs of models comparing the values of their elastic moduli. We calculated:

- the differences between two models on each pair, the mean value of these differences (m) and their standard deviation (s_d);
- the standard error of the mean difference (SE) as $SE = s_d/\sqrt{n}$, where n was the number of phantoms tested;
- the t-statistic by $T = m/SE$;
- the p-value using the tables of the t-distribution and a significant level α equal to 0.05;
- the 95 % confidence interval as $m \pm (t^* \times SE)$, where t^* is the 2.5% point of the t-distribution on $n-1$ degrees of freedom.

The confidence interval is the interval in which the mean of the differences increases or decreases with 95 % of probability. Moreover, in order to use this method, the differences between the models needed to be approximately normally distributed. Afterwards, the probability of making at least one type I error with multiple tests was calculated as $p = 1 - (1-\alpha)^n$, where n is the number of groups that were tested.

4.3 Conventional Shear Wave Elastography

4.3.1 Programmable ultrasound system

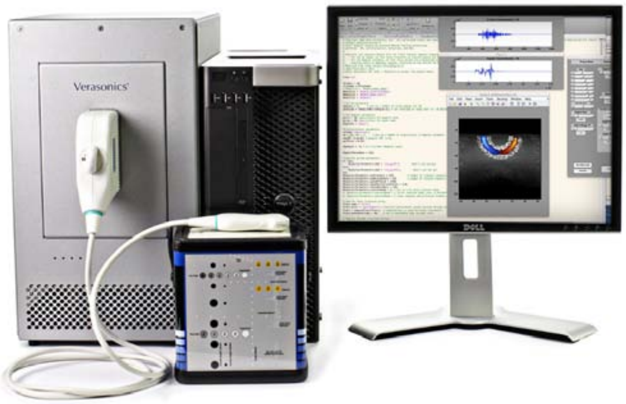

Figure 4.7: Verasonics Research System (adapted from [8]).

Shear Wave Elastography was performed using a programmable ultrasound system (V1, Verasonic Inc, Redmond, WA, USA) with a 128-element linear transducer (L7-4, Philips Healthcare, Andover, MA, USA). The Verasonics Research System is a tool for transmitting, receiving and processing ultrasound. The Verasonics Data Acquisition System (VDAS) unit consists of hardware embedded in an aluminium case connected to a host computer through a PCI Express Bus cable. A part of the data processing takes place in the host PC through Matlab programs.

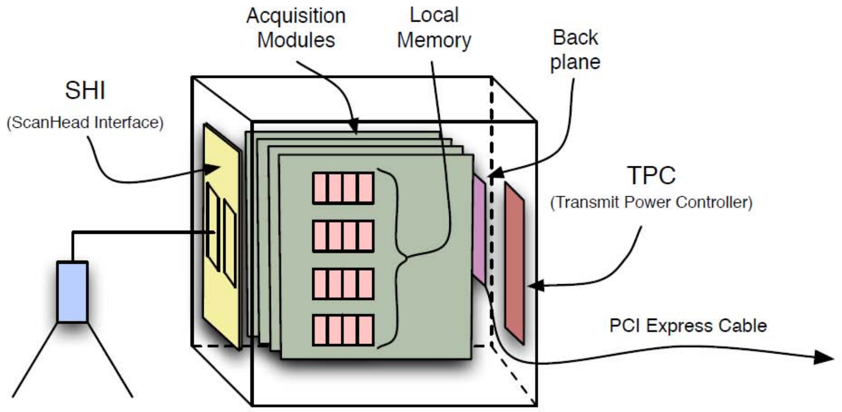

FIGURE 4.8: Components of Verasonic Data Acquisition System (adapted from [8]).

As shown in Figure 4.8, VDAS unit hardware is composed of several components:

- *Scanhead Interface*: contains the scanhead connectors;
- *Acquisition Modules*: contain the circuits for transmitting and receiving the signals;
- *Transmit Power Controller*: contains the high voltage power supply for the transmitters.

The four board system, which was used in this study, supports 256 and 128 channels for transmission and reception respectively. In table 4.3 are listed the main structures used in programming the machine.

Structure	**Description**
Resource.Parameters	Specify some system parameters
Trans	Specify the characteristic of the transducer
SFormat	Define the geometry of the acquisition regions
PData	Specify the location of the pixel data array
Resource.RcvBuffer	Define storage space for the RF data
Resource.ImageBuffer	Reconstructing an image
TW	Transmission wave forms
TX	Transmission description, including delays and apodization
TGC	Time Gain Compensator
Receive	RF receiving details
Recon	Reconstruction instruction, including which data to reconstruct
ReconInfo	Reconstruction info, describing the type of reconstruction
Process	Data processing, such as image display and shear wave elastography calculations
SeqControl	Sequence control to create loops and delays in the event sequence, as well as other miscellaneous actions
Event	Sequence of event to process when running
UI	User Interface

Table 4.3: List of structures (adapted from [11])

4.3.2 Post-Processing

Figure 4.9 shows the direction of the ultrasonic pushing beam compared to the plane of the B-mode images in conventional SWE.

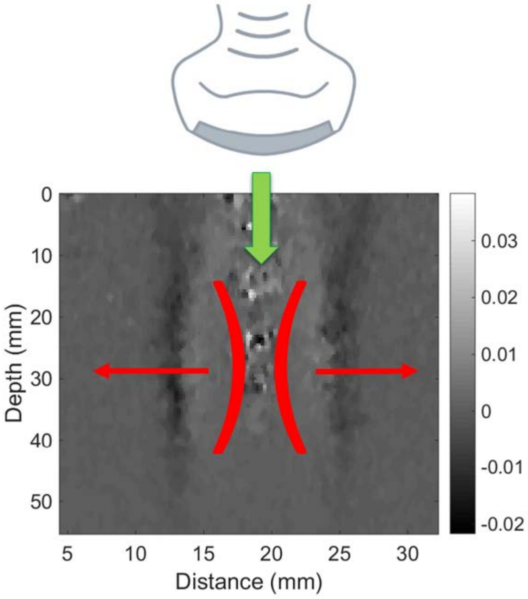

FIGURE 4.9: Pushing beam direction (green arrow) compared to the shear wave propagation direction (red arrows) in conventional SWE. The red brackets ")(" represent the focal point of the transducer.

An estimation of tissue stiffness can be done using shear wave velocity. From the IQ data, which encodes information upon a sine wave and is obtained from the Verasonic system, shear wave propagation velocity can be calculated.

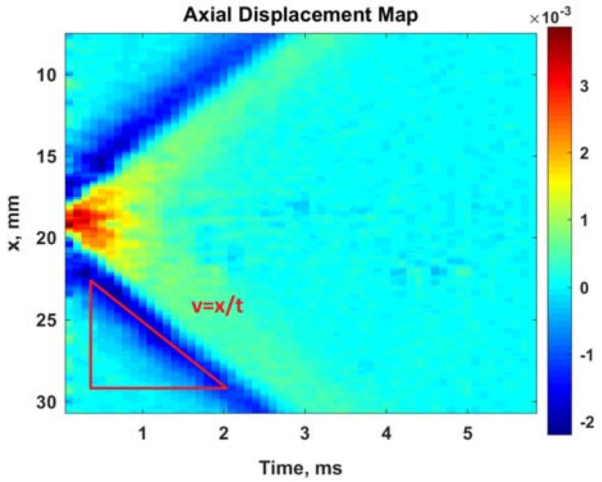

FIGURE 4.10: Shear wave propagation represented by an axial displacement map. Pixel intensities encode the axial displacement along the pushing beam.

The IQ data stores the B-mode images with a time resolution of 0.1 ms. By calculating the mean values along the columns for each frame we obtain the axial displacement displayed in Figure 4.10 where the x-axis and y-axis correspond to the time and the direction perpendicular to the ultrasonic beam respectively. The pixel intensity depends on the value of the displacement in the direction of the beam (Figure 4.11). A quick estimation of the velocity can be done by looking at the image and using the formula $v = x/t$ (where x is the displacement and t is the time), while, for an automated post-processing, the Radon transform is preferred.

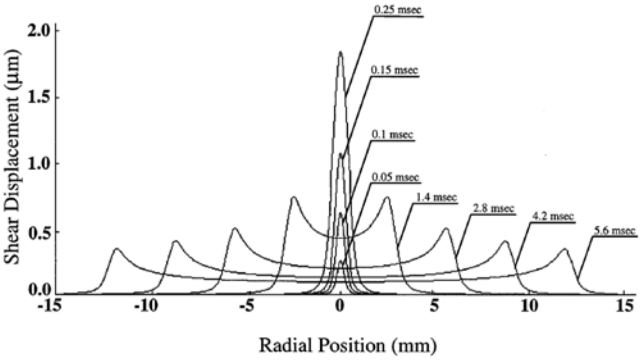

Figure 4.11: Temporal and spatial behaviour of axial displacement along the radial direction at the focal of the transducer (adapted from [5])

The Radon transform is a projective transformation of a two-dimensional function $f(x, y)$ onto the polar coordinate space (θ, s) [9]:

$$R_\theta(s) = \int_{-\infty}^{+\infty} \int_{-\infty}^{+\infty} f(x, y)\delta(xcos\theta + ysin\theta - s)dxdy \tag{4.5}$$

where $R_\theta(s)$ is a projection of $f(x, y)$ on the axis s of θ direction. The function $f(x, y)$ is the integral along the line perpendicular to θ direction [9]. A schematic representation of this formulation is given by Figure 4.12.

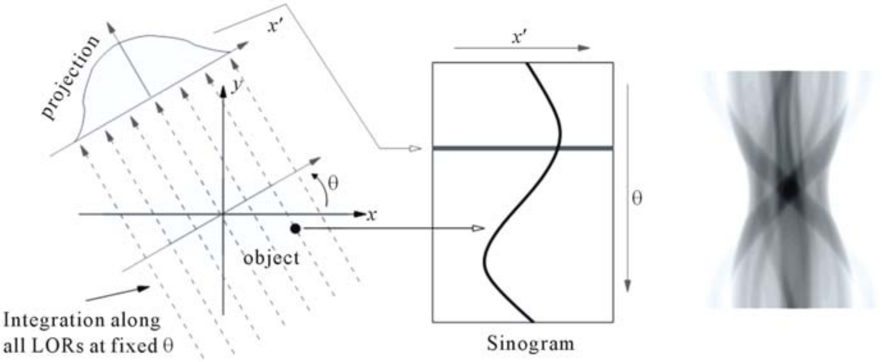

FIGURE 4.12: Illustration of a projection and a sinogram in which each projection fills a single row of θ in the sinogram. The right image shows the sinogram of a general object (LORs are the lines of response) (adapted from [9])

Applying this transform to an axial displacement map and finding the angle θ that minimizes (or maximizes) $R_\theta(s)$ equals to identify the direction of the line representing the wave propagation over the time. In Figure 4.10 we can detect the tilted angle θ of the blue line and, knowing the spatial and temporal resolution, we can find the velocity. Figure 4.13 shows an example of a projection and a sinogram of the upper of the axial displacement map.

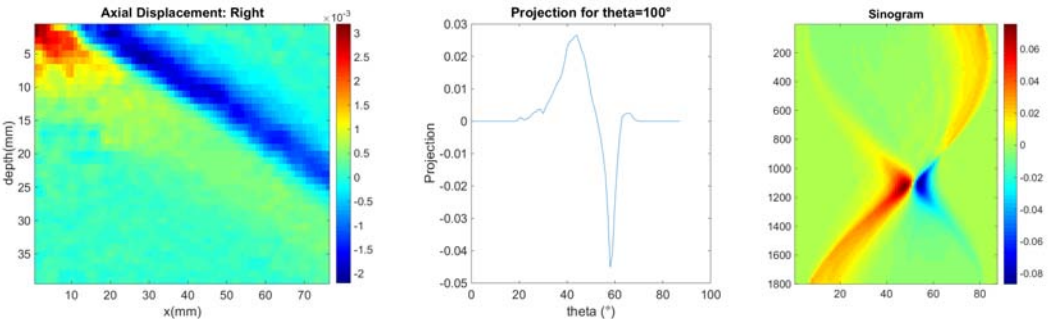

FIGURE 4.13: Illustration of a projection and a sinogram in a axial displacement map.

Shear wave propagation velocity was measured in different directions in the same B-mode image. With conventional SWE we can only track the displacement perpendicular to the beam losing information about the displacement along the beam. The velocities were obtained for 0, 15, 30, 150, 165 and 180 degrees assuming the others according to symmetry properties. Figure 4.14 shows an example of B-mode image of the shear wave displacement. Calculating the mean values of the displacement along the red lines, it is possible to estimate the shear wave propagation velocity along these lines.

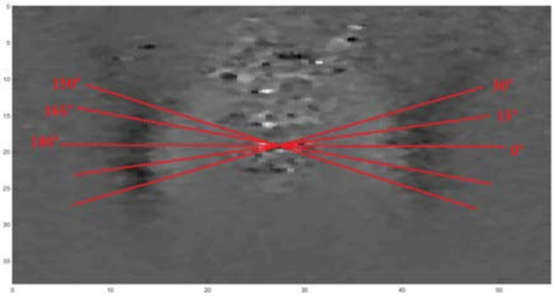

Figure 4.14: Example of B-mode image used to measure shear wave propagation velocities in different angles with conventional SWE (Phantom 11). Pixel intensities encode displacement values.

Moreover, in order to verify that the procedure described in the phantom construction gives rise to a homogeneous phantom, shear wave propagation velocities were measured in different positions in the same phantom. In particular, the test was done on phantom 6 and the velocities were estimated in six positions in the transverse direction and three in the longitudinal direction. For the other phantoms, less measurements were performed (4-6 in total) in order to calculate the standard deviation of the velocities.

4.4 Dual Probe Shear Wave Elastography

To enable capture of multiple wave motion, a novel setup consisting of two transducer heads was created. Dual-probe Shear Wave Elastography was performed using the Verasonic ultrasound system and two 128-element linear transducers (L7-4, Philips Healthcare, Andover, MA, USA). A support was made in order to tilt the phantom of 45 degrees and place the two probes 90 degrees from each other. Looking at Figure 4.15, the left transducer was used to send a focused ultrasonic beam in a direction perpendicular to the fibers while the right one was used to send ultrasonic plane waves in order to obtain sequenced B-mode images with a temporal resolution of 0.1 ms.

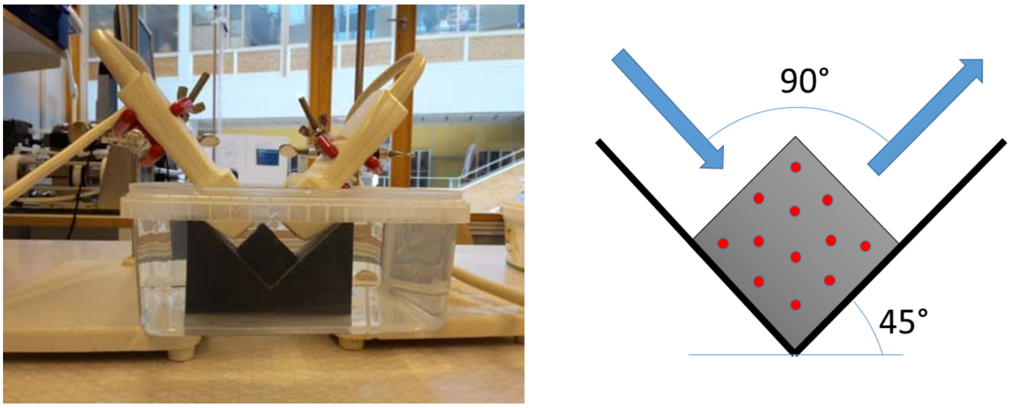

(a) (b)

FIGURE 4.15: Figure (a) was taken at KTH lab and shows the set-up for the dual-probe SWE. The sample was placed in a tank filled with water and on a support made of an absorbing material. A transducer was used to send the ultrasonic push (left probe) and another one was used to form the sequenced B-mode images (right probe). Figure (b) is a schematic representation of what is shown in Figure (a). The red dots show the direction of the fibers.

The set-up described above is in line with the Finite Element (FE) study made by Rouze et al. [10] about shear wave propagation in an incompressible, transversely isotropic medium. First, considering the particle displacement along the direction of the ultrasonic beam equals to use a single transducer for both transmission and reception. This pure transverse (PT) wave mode is theoretically described by [10]:

$$\rho v_{PT}^2 = \mu_T sin^2\theta + \mu_L cos^2\theta \tag{4.6}$$

The constants μ_T and μ_L are the shear moduli in transverse and longitudinal directions respectively and were estimated through conventional SWE.

Second, considering the bi-dimensional particle displacement a dual probe set-up is needed. This quasi-transverse (QT) wave mode is theoretically described by [10]:

$$\rho v_{QT}^2 = \mu_L + 4(\frac{E_L}{E_T}\mu_T - \mu_L) sin^2\theta cos^2\theta \tag{4.7}$$

where μ_T and μ_L were estimated trough conventional SWE and the ratios between the elastic moduli E_L/E_T were calculated through the mechanical tests.

4.4.1 Post-processing

Figure 4.16 shows the direction of the pushing beam compared to the plane of the B-mode image and can be compared with Figure 4.9 to see the difference between conventional and dual-probe SWE. Since in dual-probe SWE two transducers are placed perpendicularly from each other, also the beam and the imaged plane are perpendicular.

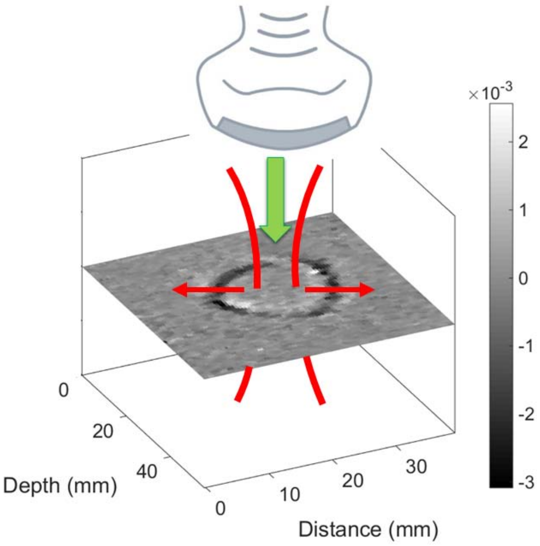

FIGURE 4.16: Pushing beam direction (green arrow) compared to shear wave propagation direction (red arrows) with dual-probe SWE. The red brackets ")(" represent the focal point of the transducer.

In the single-probe set-up, the shear wave group velocities $v'_{PT}(\theta)$ were measured along 6 directions deriving the other 4 from symmetry properties. In the same way, shear group velocities $v'_{QT}(\theta)$ were estimated in the dual-probe set-up. In this case, due to a different shape of the wave propagation displacement, it was possible to measure the speed along an additional direction (7 calculated and 5 derived velocities). In particular, the velocities were obtained for 0, 30, 60, 90, 120, 150 and 180 degrees assuming the others from symmetry properties. Figure 4.17 shows an example of B-mode image of the shear wave displacement measured using dual-probe SWE. Calculating the mean values of the displacement along the red lines, it is possible to estimate the shear wave propagation velocity along these lines.

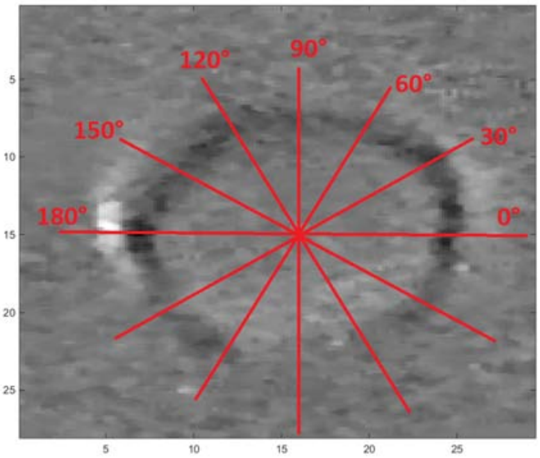

FIGURE 4.17: Example of B-mode image used to measure shear wave propagation velocities in different angles with dual-probe SWE (Phantom 11). Pixel intensities encode displacement values.

The aim was to compare the curves derived from the theoretical results ($v_{PT}(\theta)$ of Equation 4.6 and $v_{QT}(\theta)$ of Equation 4.7) with the curve obtained from phantom measurements. Figure 4.18 shows an example of the comparison between the theoretical group velocities propagation and the velocities calculated with FE models [10]. In our study the theoretical velocities were compared with the ones calculated from the displacement results of shear wave elastography.

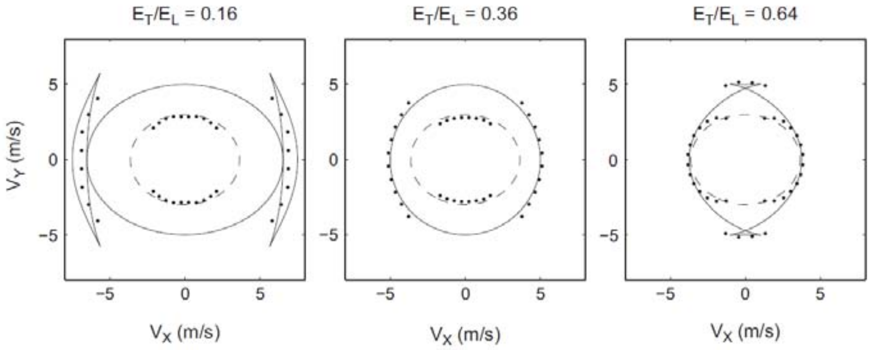

FIGURE 4.18: Parametric plots of theoretical group propagation velocities. Pure-transverse (dashed) and quasi-transverse (solid) propagation modes calculated using $\mu_L = 25kPa$, $\mu_T = 9kPa$ are compared with the velocities calculated with the displacement results of the Finite Element model (data points) (produced and published by Rouze et al. [10])

In order to have a quantitative estimation of the goodness of the fitting, a statistical test was performed on each phantom. The Residual Sum of Squares (RSS) was calculated by the squared differences between parametric and measured data as:

$$RSS = \sum_{i=1}^{n} (y_i - f(x(i)))^2 \tag{4.8}$$

where y_i is the measured data, $f(x(i))$ is the parametric curve and n is the number of data points. For each phantom, the RSS was calculated for both conventional and dual-probe SWE.

A more detailed statistic was done for phantom 4 because it was giving the best results in the RSS test for the quasi-transverse propagation mode. While for all the other phantoms only a single measurement was performed using the dual-probe set-up, phantom 4 was tested two more times in order to have a total of three velocities for each direction of propagation. Afterwards, the RSS values were calculated for the three measurements in order to see how much they were varying for different measurements in the same phantom.

Another statistical test was performed using both the velocities obtained with dual-probe set-up and the values of the shear moduli obtained with conventional SWE. The method of the weighted non-linear least square (WNLLS) was used and the data was fitted with Equation 4.7. In particular, the Matlab script was receiving in input the velocities calculated with dual-probe SWE and the shear moduli calculated with conventional SWE and was using these parameters to estimated the value of the ratio E_T/E_L that was giving the best fitting.

Chapter 5

Results

5.1 Mechanical tests

The stress-strain curves obtained from the mechanical tests (Figure 5.1) were used to fit three different elastic models: linear interpolation, Neo-Hookean and Mooney-Rivlin.

Figure 5.1 (a) and (b) show the four measurements in the transverse direction and the two measurement in the longitudinal direction respectively.

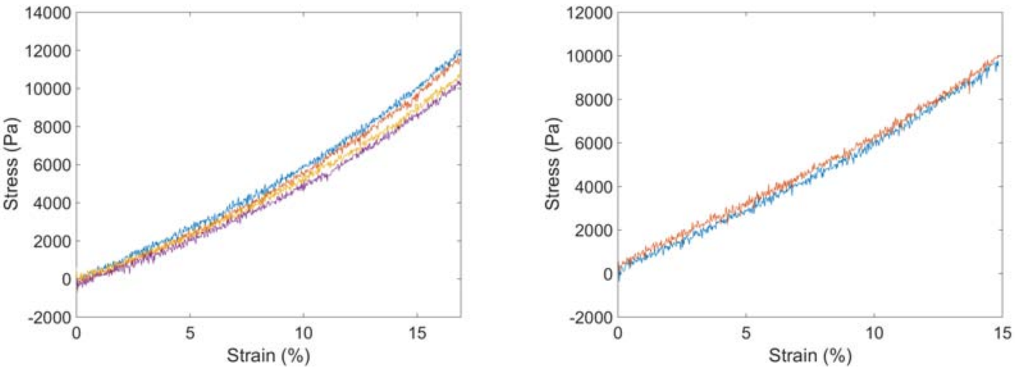

(a) (b)

Figure 5.1: Stress-strain curves in the plane of isotropy (a) and in longitudinal direction (b) for phantom 2. For each phantom, 4 measurements in the plane of isotropy and another 2 in the longitudinal direction (plotted in different colours in each graph) were performed in order to obtain a more accurate estimate of the elastic moduli and validate the transverse isotropy.

Figure 5.2 presents an example of the data points (blue) compared to the three fitted curves (red) for a measurement in the plane of isotropy: linear interpolation (Figure 5.2 (a)), Neo-Hookean (Figure 5.2 (b)) and Mooney-Rivlin (Figure 5.2 (c)).

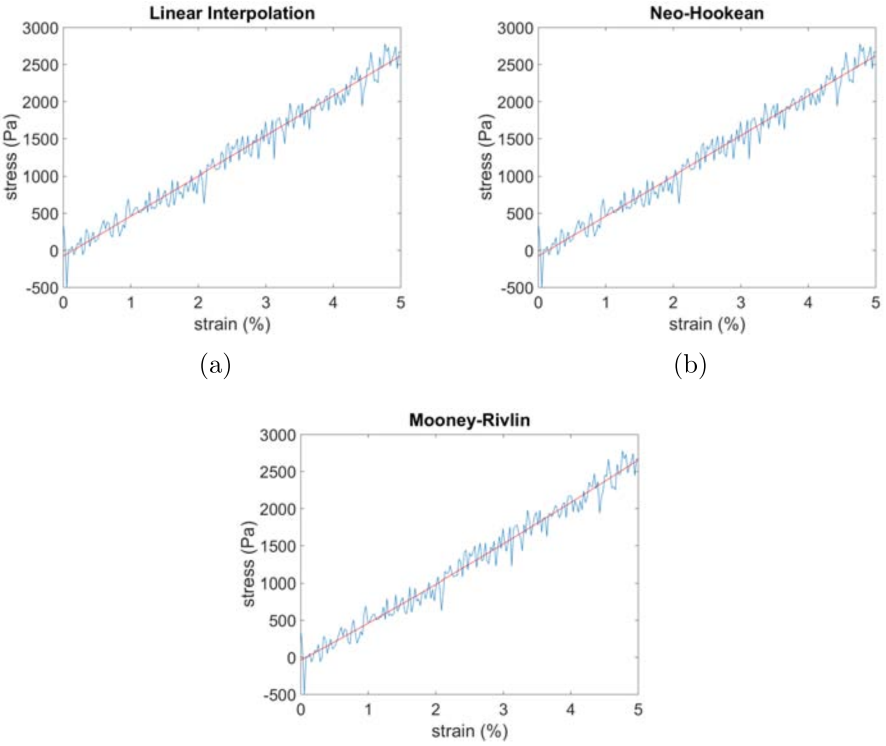

(a)

(b)

(c)

FIGURE 5.2: Example of stress-strain curves fitted using linear interpolation (a), Neo-Hookean (b) and Mooney-Rivlin (c) models for phantom 2. In all the three plots, the data points and the fitted curves are represented with blue and red lines respectively.

The values of E_T and E_L for all the phantoms are reported in Tables 5.1 and 5.2 respectively (with relative standard deviations) and were calculated with the three constitutive models. Each E_T is the average of the four measurements in the plane of isotropy and likewise each E_L is the average of the two measurements in the longitudinal direction. For a better understanding, we chose to present the results clustering the phantoms according to their PVA density, i.e. presenting first the results of phantoms 1, 2, 3, 4 and 5 made of 7 % of PVA and then the ones for phantoms 6 and 7 made of 5% of PVA.

Phantom	Linear Interpolation E_T(kPa)	Neo-Hookean E_T(kPa)	Mooney-Rivlin E_T(kPa)
1	40.7±3.8	40.7±3.8	33.8±4.3
2	48.9±4.2	48.9±4.3	42.3±4.7
3	42.6±6.1	42.6±6.2	36.7±6.9
4	33.8±4.5	33.8±4.5	30.9±10.9
5	44.2±7.4	44.2±7.4	35.4±3.2
6	18.1±5.0	18.1±5.0	12.1±15.7
7	17.9±6.6	17.8±6.6	17.2±10.3

Table 5.1: Elastic moduli in the plane of isotropy calculated with three different constitutive models: linear interpolation, Neo-Hookean and Moonley-Rivlin. Phantom 6 and 7 are made of a lower PVA density.

Phantom	Linear Interpolation E_L(kPa)	Neo-Hookean E_L(kPa)	Mooney-Rivlin E_L(kPa)
1	47.0±1.4	47.0±1.4	39.8±2.2
2	55.3±3.9	55.3±3.9	54.7±4.8
3	51.9±0.3	51.9±0.3	57.0±6.1
4	52.3±7.4	52.3±7.4	62.0±1.5
5	52.8±0.3	52.8±0.3	56.5±5.4
6	25.5±0.3	25.5±0.3	18.2±8.4
7	19.1±3.3	19.1±3.3	31.5±7.0

Table 5.2: Elastic moduli in longitudinal direction calculated with three different constitutive models: linear interpolation, Neo-Hookean and Moonley-Rivlin. Phantom 6 and 7 are made of a lower PVA density.

After calculating the elastic moduli, the three data sets (Linear Interpolation (LI), Neo-Hookean (NH) and Mooney-Rivlin (MR)) were compared and clustered in three groups: LI vs NH, LI vs MR and NH vs MR. The results of paired t-tests state with 95% confidence that:

- the difference between E_T calculated with linear interpolation and Neo-Hookean model lies between 17 and 33 Pa;
- the difference between E_L calculated with linear interpolation and Neo-Hookean model lies between 17 and 38 Pa;
- the difference between E_T calculated with linear interpolation and Mooney-Rivlin model lies between 982 and 9853 Pa;
- the difference between E_L calculated with linear interpolation and Mooney-Rivlin model lies between -9400 and 4901 Pa;
- the difference between E_T calculated with Neo-Hookean and Mooney-Rivlin model lies between 961 and 9823 Pa;
- the difference between E_L calculated with Neo-Hookean and Mooney-Rivlin model lies between -9425 and 4870 Pa;

The p-values with α equal to 0.05 were also measured and reported in Table 5.3. If the p-values were lower than 0.05 than the two groups were considered different.

Group	p-value (E_T)	p-value (E_L)
LI vs NH	1	1
LI vs MR	0.15	0.009
NH vs MR	0.15	0.009

TABLE 5.3: P-values for each group (Linear Interpolation (LI), Neo-Hookean (NH) and Mooney-Rivlin (MR)

The probability of making at least one type I error with 3 groups is $1–(1-0.05)^3 = 0.143$ which means that the chance of incorrectly rejecting the null hypothesis is about 1 in 7. Following these results, the linear interpolation model was chosen partly due to computational simplicity and partly due to the similarity in results with the evaluated hyperelastic models. For more details on this, see section 6.2.

In order to verify the transverse isotropy of the phantoms, the ratios E_T/E_L were calculated and reported in Table 5.4.

Phantom	E_T (kPa)	E_L (kPa)	E_T/E_L
1	40.7±3.8	47.0±1.4	0.87
2	48.9±4.2	55.3±3.9	0.88
3	42.6±6.1	51.9±0.3	0.82
4	33.8±4.5	52.3±7.4	0.64
5	44.2±7.4	52.8±0.3	0.84
6	18.1±5.0	25.5±0.3	0.71
7	17.9±6.6	19.1±3.3	0.93

Table 5.4: Elastic moduli in transverse and longitudinal directions calculated with linear interpolation. Phantom 6 and 7 are made of a lower PVA density.

Table 5.4 presents the values of the elastic moduli along the two main directions calculated with the linear interpolation model. In order to prove the transverse isotropy and the influence of PVA density, the average E_T and E_L were calculated and reported in Table 5.5. In both phantoms made of 5 and 7 % of PVA, the average E_L is 23% higher than E_T.

PVA density (%)	E_T (kPa)	E_L (kPa)
5	18.0±0.2	22.3±4.5
7	42.0±5.5	51.9±3.0

Table 5.5: Comparison between average values of E_T and E_L for phantoms made of 5 and 7 % of PVA

The mean values of E_T/E_L for a TI phantom developed with the procedure described above are 0.82 ± 0.16 and 0.81 ± 0.09 for phantoms made of 5 and 7 % of PVA respectively. Furthermore, for phantom made of 7 % of PVA the mean ratios are 0.86 ± 0.03 and 0.74 ± 0.13 for 12 and 14 hours of thawing time respectively.

The ratios between the shear moduli μ_T/μ_L are 0.78 ± 0.18 and 0.77 ± 0.11 for phantoms made of 5 and 7 % of PVA respectively.

The density was calculated with Archimedes' principle and it was 1020 $\mathrm{Kg/m^3}$ and 960 $\mathrm{Kg/m^3}$ for phantoms made of 7 and 5 % of PVA density respectively. Knowing the density and assuming $\nu_{LT} = 0.5$ [10], both shear moduli and shear wave propagation velocities in transverse (v_T) and longitudinal (v_L) direction were estimated. These values are reported in Table 5.6.

Phantom	μ_T(kPa)	μ_L(kPa)	v_T(m/s)	v_L(m/s)
1	12.98	15.6	3.58	3.93
2	15.69	18.44	3.93	4.26
3	13.41	17.31	3.64	4.13
4	10.09	17.42	3.15	4.14
5	13.97	17.61	3.72	4.17
6	5.51	8.50	2.40	2.98
7	5.83	6.36	2.45	2.56

Table 5.6: Shear moduli and estimated shear wave propagation velocities calculated assuming linear elasticity. Phantom 6 and 7 are made of a lower PVA density.

5.2 Conventional Shear Wave Elastography

Figure 5.3 shows a representative example of shear wave propagation in a phantom imaged every 0.5 ms for 6 different time frames and can be compared to the simulation presented in Figure 3.11. Pixel intensity encodes axial particle displacement along the beam axis.

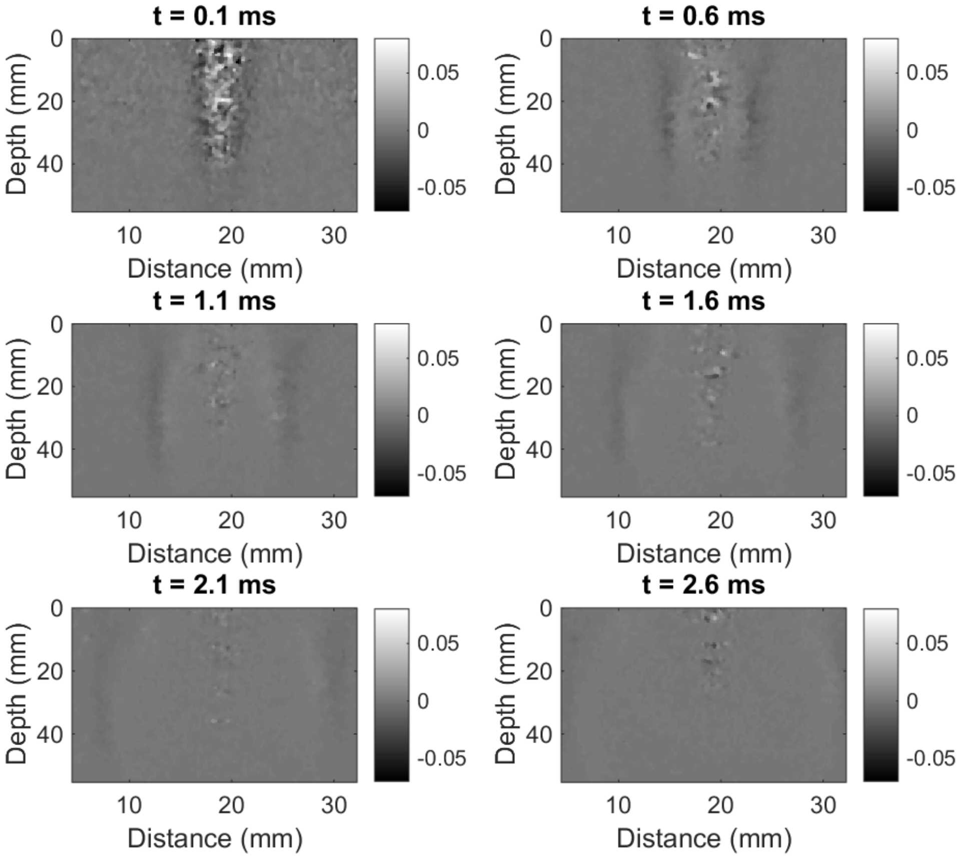

FIGURE 5.3: Example of B-mode images at different time frames showing shear wave propagation in longitudinal direction for phantom 4. The pushing beam was sent along the depth axis and the shear wave propagates perpendicularly to it. Pixel intensities are scaled equally for all the images and encode axial particle displacement.

Figure 5.4 shows an example of shear wave velocities measured in six different positions in the transverse direction (Figure 5.4 (a)) and three different positions along the longitudinal direction (Figure 5.4 (b)) for phantom 1.

Moreover, Table 5.7 presents the average values of shear wave propagation velocities for phantoms made of 5 and 7 % of PVA.

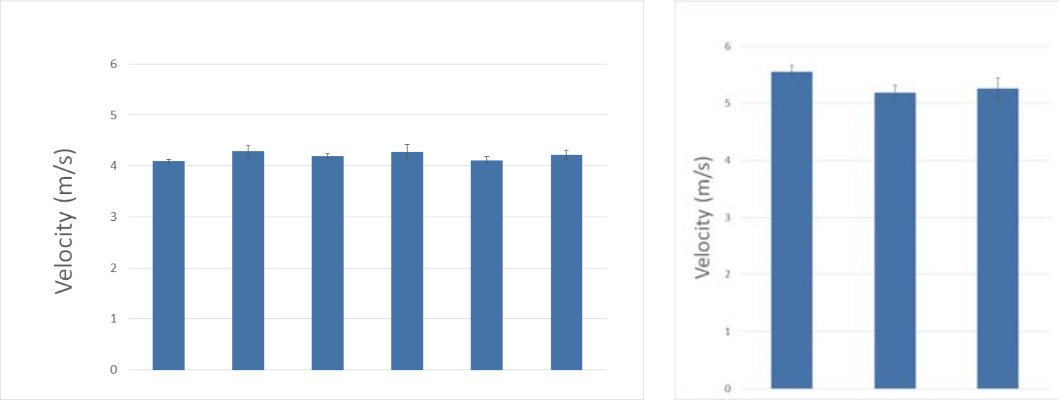

(a) (b)

FIGURE 5.4: Example of shear wave propagation velocities in different planes of isotropy (a) and in different positions along the axis of isotropy (b). The measurements were performed on phantom 1.

PVA density (%)	v_T (m/s)	v_L (m/s)
5	2.3±0.3	4.1±1.3
7	4.5±0.5	5.3±0.3

TABLE 5.7: Comparison between average values of v_T and v_L for phantoms made of 5 and 7 % of PVA

To quantify the grade of anisotropy estimated through SWE, the ratios between shear wave propagation velocities v_T/v_L have been calculated. The mean values of this ratio are 0.58 ± 0.11 and 0.86 ± 0.05 for phantoms made of 5 and 7 % of PVA respectively. Furthermore, for phantoms made of 7 % of PVA the mean ratios are 0.84 ± 0.07 and 0.88 ± 0.002 for 12 and 14 hours of thawing respectively.

The ratios between the shear moduli μ_T/μ_L are 0.34 ± 0.12 and 0.74 ± 0.09 for phantoms made of 5 and 7 % of PVA respectively.

For each phantom, shear moduli in transverse and longitudinal directions were calculated from the shear wave propagation velocities. In Table 5.8 the results of the shear wave propagation velocities and the shear moduli in the two directions are presented. The values of the standard deviation are given from repeated measurements at different positions.

Phantom	$v_T(m/s)$	$v_L(m/s)$	$\mu_T(kPa)$	$\mu_L(kPa)$	v_T/v_L
1	4.20±0.08	5.33±0.19	17.96	29.03	0.77
2	5.04±0.18	5.46±0.24	26.00	30.50	0.92
3	4.19±0.29	5.12±0.77	17.94	26.76	0.82
4	4.24±0.09	4.84±0.02	18.35	23.86	0.88
5	5.03±0.11	5.72±0.25	25.81	33.34	0.88
6	3.56±0.24	5.07±0.22	6.30	24.71	0.50
7	2.09±0.10	3.20±0.09	4.19	9.81	0.65

Table 5.8: Transverse and longitudinal shear wave propagation velocities and transverse and longitudinal shear moduli obtained with conventional Shear Wave Elastography.

5.3 Dual Probe Shear Wave Elastography

Figure 5.5 presents an example of shear wave propagation measured with a dual-probe set-up and can be compared with Figure 5.3.

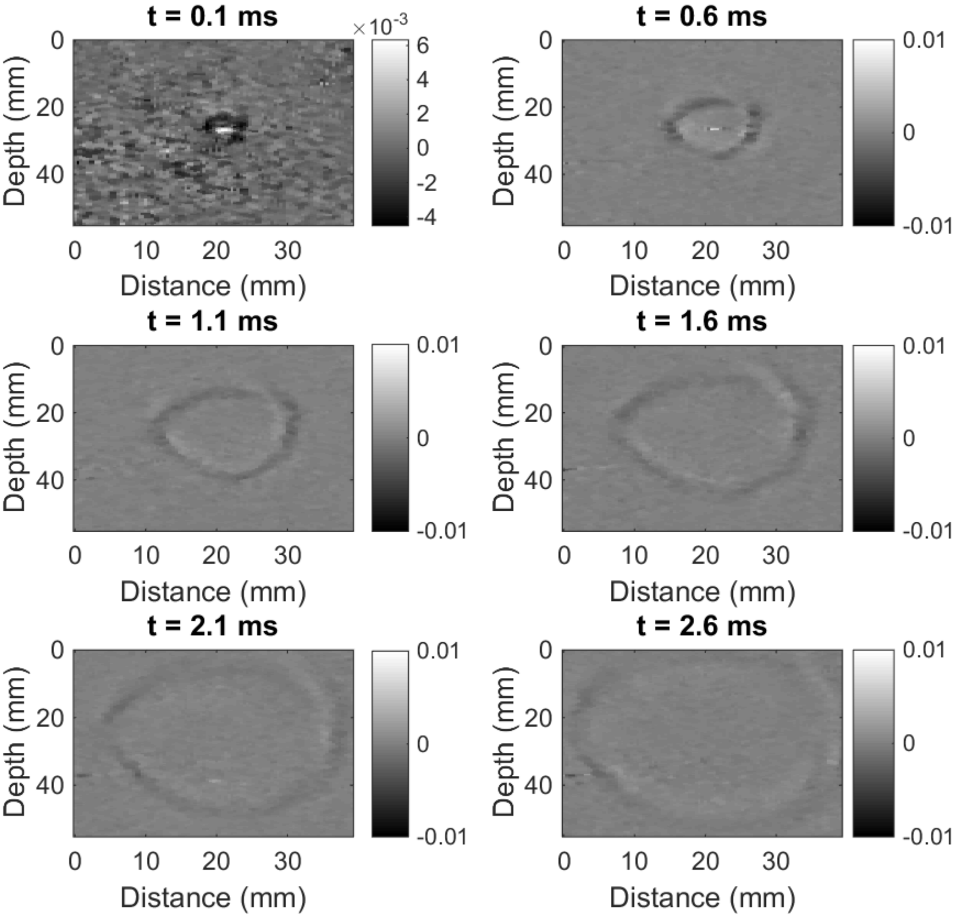

FIGURE 5.5: Example of B-mode images at different time frames showing shear wave propagation in phantom 4. The pushing beam was sent perpendicularly to the images. Pixel intensities are scaled equally for all the images a part from the top left one and encode axial particle displacement.

The following figures are parametric plots of theoretical group velocities where pure-transverse PT (red dashed) and quasi-transverse QT (blue solid) are the propagation modes. The velocities estimated using conventional and dual-probe SWE are represented by red and blue asterisks respectively. The x-axis and y-axis correspond to shear wave speed transverse to the symmetry axis and to the shear wave speed along the symmetry axis, respectively. The parameters used for the theoretical curves are gathered in Table 5.9 and refer to Tables 5.4 and 5.8.

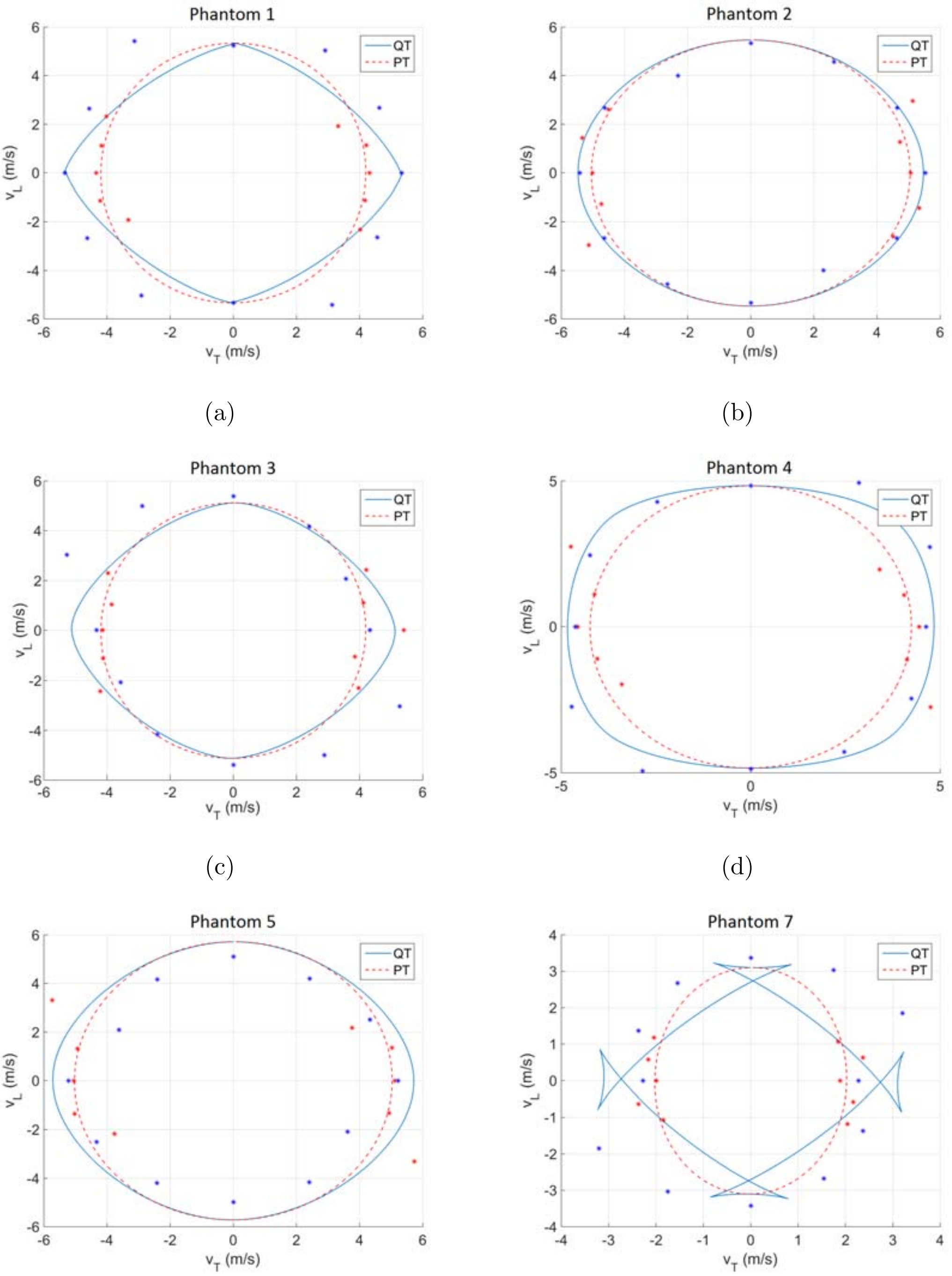

(a)

(b)

(c)

(d)

(e)

(f)

FIGURE 5.6: Parametric curves vs data points of shear wave propagation group velocities. The blue lines are the parametric curves of the quasi transverse (QT) propagation mode and the blue asterisks are the data points measured with the dual-probe set-up. The red lines are the parametric curves of the pure-transverse (PT) propagation mode and the red asterisks are the data points measured with conventional SWE.

Phantom	E_T/E_L	μ_T (kPa)	μ_L (kPa)
1	0.87	17.96	29.03
2	0.88	26.00	30.50
3	0.82	17.94	26.76
4	0.64	18.35	23.86
5	0.84	25.81	33.34
7	0.93	4.19	9.81

TABLE 5.9: Values of E_T/E_L ratios and shear moduli used to plot the parametric curves of shear waves propagation velocities. E_T/E_L were obtained from mechanical tests and the shear moduli were obtained from conventional SWE.

Figure 5.7 shows the theoretical QT (blue) and PT(red) wave propagation modes and shear wave velocities measured with dual-probe SWE (blue asterisks) in phantom 4.

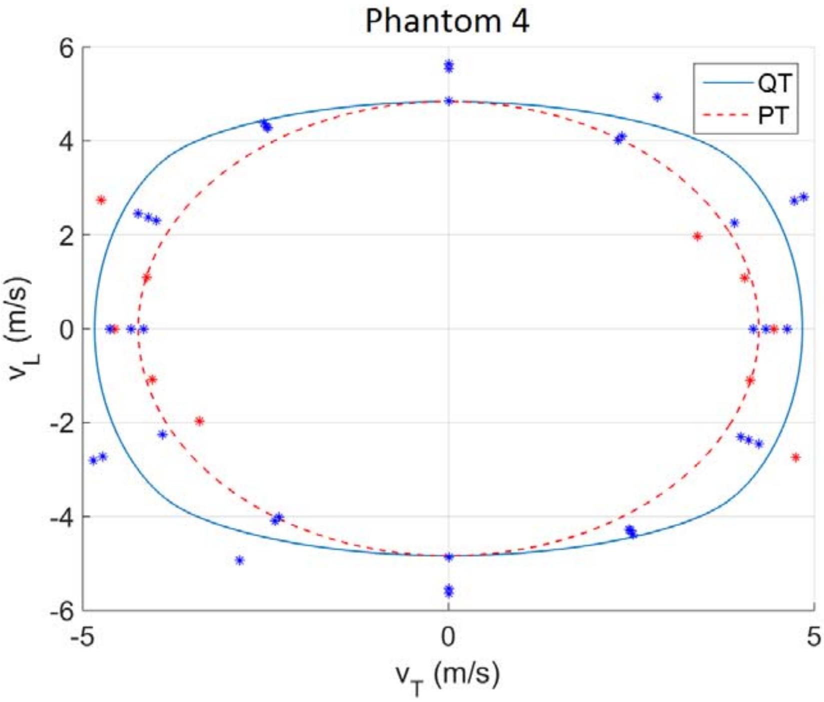

FIGURE 5.7: Parametric curves vs data points of shear wave propagation group velocities for phantom 4. The blue lines are the parametric curves of the quasi transverse (QT) propagation mode and the blue asterisks are the data points measured with the dual-probe set-up. The red lines are the parametric curves of the pure-transverse (PT) propagation mode and the red asterisks are the data points measured with the conventional SWE.

The results of the statistical tests performed to have a quantitative measure of the goodness of the fitting are reported in Table 5.10 in terms of the residual sum of squares (RSS) for both pure-transverse and quasi-transverse propagation modes. Lower values of the RSS represent a lower deviation of the data points from the theoretical curves, thus a better fitting.

Phantom	RSS-PT $(\text{m/s})^2$	RSS-QT $(\text{m/s})^2$
1	0.63	2.90
2	0.81	0.69
3	1.70	3.72
4	0.30	5.83
5	1.49	0.51
7	2.69	4.48

Table 5.10: Residual sum of squares (RSS) values for both pure-transverse (PT) and quasi-transverse (QT) propagation modes

Table 5.11 presents the results of the RSS test for phantom 4 where tests 1, 2 and 3 correspond to the data point measured with dual-probe. Lower RSS values mean a lower deviation of the theoretical curves from the curves estimated using data points, thus they indicate a better fitting.

Test's number	RSS $(\text{m/s})^2$
Test 1	0.51
Test 2	2.49
Test 3	2.32

Table 5.11: Results of the RSS test for Phantom 4.

Figure 5.8 presents the plots of QT parametric curves and their predictions calculated with WNLLS. Table 5.12 shows the values of E_T/E_L estimated from the predicted curves.

Phantom	Predicted E_T/E_L	Measured E_T/E_L
1	0.62	0.87
2	0.85	0.88
3	0.67	0.82
4	0.43	0.93
5	0.77	0.64
7	0.78	0.84

TABLE 5.12: Values of E_T/E_L estimated with WNLLS and measured with mechanical tests.

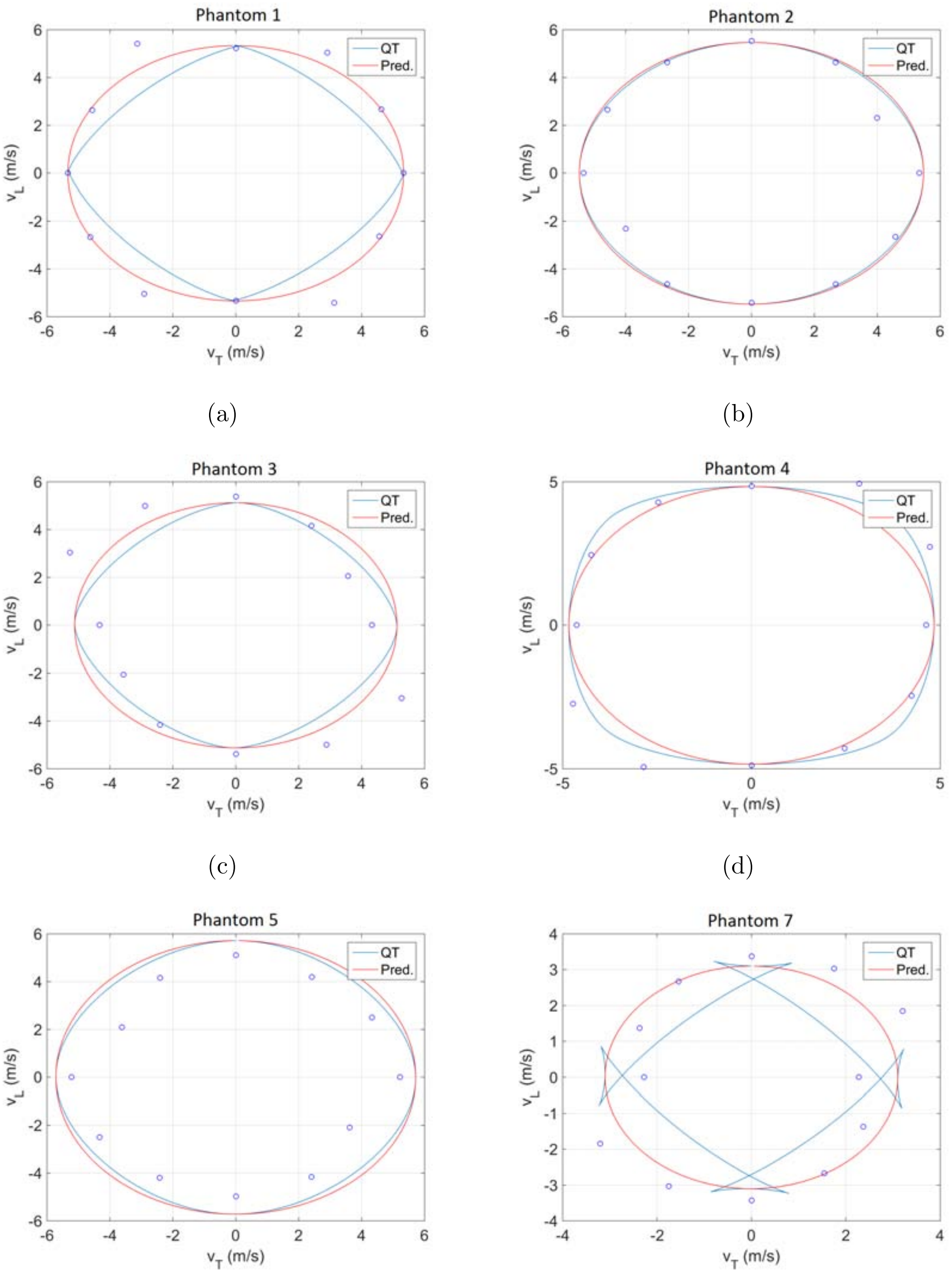

(a) (b)

(c) (d)

(e) (f)

Figure 5.8: Quasi-transverse parametric curves vs curves predicted using WN-LLS. The blue lines are the parametric curves of the quasi transverse (QT) propagation mode and the blue circles are the data points measured with the dual-probe set-up. The red lines are the curves predicted using the data points and the shear moduli estimated with conventional SWE.

Chapter 6

Discussion

In this work, a way of assessing multiple shear wave propagation modes on a developed transversely isotropic phantom using dual-probe Shear Wave Elastography was presented. Initial results showed a good agreement between experimental data and theoretical predictions indicating the ability of SWE as a measurement tool for more complex analysis of mechanical behaviour even for transversely isotropic tissue.

6.1 Phantom Construction

During the development of phantoms made of different PVA density, a value of 7% was chosen as a trade-off between phantom behaviour in SWE and mechanical tests. The technique used for the phantoms construction was adapted to the study made by Chatelin et al. [36] where the phantoms were made of 5 % of PVA density and stretched to 180% of their initial length. Phantoms made of 5% of PVA were more easy to stretch without rupture but their low consistence led to difficulties in acquiring flat surfaces specimens and, as a consequence, mechanical tests resulted less reliable. For this reason, phantoms made of 7% of PVA were used in this work and suggested for studies which require compression tests. However, some phantoms made of 5% of PVA were developed as comparison. Moreover, the phantoms were big enough to avoid guided waves in line with the design of Chatelin et al. [36].

6.2 Mechanical tests

According to the results reported in Tables 5.1 and 5.2, linear interpolation and Neo-Hookean models looked similar from each other while Mooney-Rivlin model gave different values of the elastic moduli with a higher standard deviation. These considerations were supported by the results of the statistical tests which showed a high correspondence between linear interpolation and Neo-Hookean model. In fact, the two models differed on average by $25-27$ Pa which was very low compared to the magnitude of the elastic moduli. The same conclusion could not be drawn comparing these two models with Mooney-Rivlin model because of the higher average values of their differences and the higher width of their confidence intervals. The p-values reported in Table 5.3 showed the relations between pairs of data sets. In particular, assuming $\alpha = 0.05$, two groups were considered different when the p-value was lower than α. According to these values, linear interpolation and Neo-Hookean model gave the same results (p=1) for both E_T and E_L while Moonley-Rivlin gave results similar to the other two models for E_T (p=0.15) but was different for E_L (p=0.009). Therefore, the p-values confirmed what obtained with the confidence intervals. With three groups, the probability of making at least one type I error was 0.143 which means that the chance of incorrectly rejecting the null hypothesis was about 1 in 7. An incorrect rejection leads one to conclude that two data sets are different when in fact they are not. When the number of groups is higher, this probability increases and it is better to consider other types of statistical tests like ANOVA, which maintains the type I error probability at a constant level. Looking at the stress-strain curves, Moonley-Rivlin model was giving a good fitting when considering the results until higher strain (10-15%) but generally showed a higher deviation from the data points at lower strain (0-3 %). Therefore Moonley-Rivlin model was excluded from the study and linear interpolation was selected to represent the mechanical behaviour of the phantom material.

Table 5.4 demonstrated that the procedure described in Chapter 4 gave rise to transversely isotropic phantoms and confirmed what expected from the theory. First, each phantom had a higher elastic modulus in longitudinal direction compared to the one in the plane of isotropy. Second, phantoms made of 5 % of PVA had an average E_T of 18.0 ± 0.2 kPa and E_L of 22.3 ± 4.5 kPa while phantoms made of 7 % of PVA had an average E_T of 42.0 ± 5.5 kPa and E_L of 51.9 ± 3.0 kPa (Table 5.5). These values also proved that increasing the PVA density increased also phantom stiffness and thus its elastic modulus in both directions.

The ratios between the elastic moduli E_T/E_L were calculated in order to have a parameter which described the grade of anisotropy reached with different procedures. The three clusters of phantoms divided by thawing time and PVA density were examined separately and gave 0.86 ± 0.03 (12h thawing time and 7% PVA), 0.74 ± 0.13 (14h thawing time and 7% PVA) and 0.82 ± 0.15 (14h thawing time and 5% PVA). At first sight, these values indicated that increasing the thawing time increased the anisotropic behaviour of the phantom but Table 5.4 showed that the low value obtained for 14h of thawing time and 7% of PVA was strongly influenced by the ratio in phantom 4. Therefore, we cannot conclude that these parameters influenced the grade of anisotropy.

Comparing these results with Table 3.1, our phantoms show similarities with the elastic moduli of healthy soft tissue like kidney, breast, prostate and liver ($E \simeq 0.5 - 70$ kPa) but they are too soft to represent tendon ($E \simeq 800$ kPa). The elastic modulus of muscle is more variable and depends of the state of the muscle during the measurement.

6.3 Conventional SWE

In line with the mechanical tests, the results obtained using SWE showed that all the phantoms had a transversely isotropic behaviour. For each phantom, shear wave propagated at a higher velocity along the longitudinal direction than in the plane of isotropy. In particular, phantoms made of 5 % of PVA had an average v_T of 2.3 ± 0.3 m/s and v_L of 4.1 ± 1.3 m/s while phantoms made of 7 % of PVA had an average v_T of 4.5 ± 0.5 m/s and v_L of 5.3 ± 0.3 m/s (Table 5.7). As for the elastic modulus, shear wave propagation velocity increased with PVA density.

As for the ratio between the elastic moduli, the ratios between shear wave propagation velocities v_T/v_L were calculated. At first sight, these values indicated that the anisotropic behaviour of the phantoms did not change with thawing time but was stronger in softer phantoms. This consideration was not supported by the results obtained with the mechanical tests thus the ratios between estimated shear moduli were calculated. In both cases, shear moduli were estimated from indirect measurements and were influenced by approximations like phantom density and isotropy along longitudinal direction. For phantoms made of 7% of PVA, μ_T/μ_L varied between 0.74 (SWE) and 0.77 (mechanical tests) while for phantoms made of 5% of PVA μ_T/μ_L varied between 0.34 (SWE) and 0.78 (mechanical tests). For phantoms made of 5% of PVA the high difference between SWE and mechanical test can be due to the difficulty in perform mechanical tests. In general, shear moduli estimated with conventional SWE were higher than the ones estimated through mechanical tests.

Chatelin et al. [36] obtained values of shear wave propagation velocities which were approximately 1.95 m/s and 3.2 m/s in transverse and longitudinal directions respectively compared to 2.3 m/s and 4.1 m/s obtained in this study. However, the applied strain during the stretching was 0.80 for Chatelin and 0.60 for this study thus the previous results were not supposed to be identical.

Mechanical Tests vs Conventional SWE

Both mechanical tests and conventional SWE proved the transverse isotropy of the phantoms showing a higher stiffness along the longitudinal direction. Nevertheless, the results of these two tests did not perfectly coincide. For phantoms made of 5 % of PVA, the shear moduli were $\mu_T = 5.67$ kPa and $\mu_L = 7.43$ kPa for mechanical tests and $\mu_T = 5.25$ kPa and $\mu_L = 17.26$ kPa for conventional SWE. Likewise, in the study made by Chatelin et al. [36], the shear moduli were $\mu_T = 4.31$ kPa and $\mu_L = 6.28$ kPa for dynamic mechanical analysis and $\mu_T = 3.8$ kPa and $\mu_L = 10.5$ kPa for conventional SWE. In both cases one can see the difference between the values of the mechanical tests and SWE. This could be due to assumptions made in order to simplify the calculations, for example isotropy along the longitudinal direction, viscosity or incompressibility. In general, our study shows slightly higher shear moduli compared to the study made by Chatelin.

In this project, only transversely isotropic phantoms were considered leaving aside tests on living biological tissue but other studies measured the elastic parameters in different kind of phantoms and living tissue. For example, the shear moduli of bovine muscle are $\mu_T = 8.9$ kPa and $\mu_L = 17.2$ kPa [37] and the shear moduli of pork tenderloin are $\mu_T = 5.9$ kPa and $\mu_L = 13.3$ kPa [39]. The study made by Aristizabal et al. [39] shows that the transverse isotropy can be obtained also incorporating fibrous or fishing line material in porcine gelatin. The shear moduli are, in the first case, $\mu_T \simeq 10 - 12$ kPa and $\mu_L \simeq 15 - 17$ kPa and, in the second case, $\mu_T \simeq 5 - 8$ kPa and $\mu_L \simeq 8 - 12$ kPa depending on the gelatin concentration. However, as already indicated by Chatelin [36], a phantom made of PVA is particularly recommended in researches focused on ultrasound-based elastography because it avoids acoustic impedance losses which exist in phantoms made of a mixture of hydrogel and other materials.

6.4 Dual-probe SWE

The data points collected through SWE in a dual-probe set-up showed a good agreement with the theoretical curves estimated using the results obtained from both mechanical and conventional SWE tests. First of all, it was interesting to note the difference in shape of the wave imaged with one and two transducers. This can be seen comparing Figure 5.3 and 5.5. In fact, while conventional ultrasound can only track the shear wave propagation perpendicular to the beam axis, a dual-probe set-up can track the displacement in several directions at the same time.

The main results obtained with this method were the curves presented in Figure 5.6. These curves were in line with the theoretical curves obtained by Rouze et al. [10]. In general, the shape of the parametric curves was varying according to the E_T/E_L ratio and the shear moduli. As mentioned before, it was difficult to perform mechanical tests on phantom 7 due to its low stiffness and thus the shape of its quasi-transverse propagation mode was strongly influenced by its high value of E_T/E_L.

The divergence from the measured data was also proven by statistical tests which gave a quantitative evaluation of the goodness of fits. As shown in Table 5.10, for pure-transverse mode RSS values were varying from 0.30 for phantom 7 to 2.69 for phantom 5 showing a good agreement between parametric curves and measured data for phantom 7 and a high RSS for phantom 5 due to the difference along the 150 degrees direction (see Figure 5.6 (f)). For quasi-transverse propagation mode, RSS values were varying between 0.51 for phantom 4 and 5.83 for phantom 7. Phantom 4 gave the best agreement between measured data and theoretical curves in QT mode and thus it was tested two more times to obtain a statistical description of the distribution of the data point around the theoretical curve (Figure 5.7). The results in Table 5.11 showed that, for different measurements, the RSS values were varying from 0.51 to 2.49 and highlighted the advantages of collecting repeated measurements when using the data sets to describe the mechanical properties of a tissue.

Figure 5.6 indicated the possibility of measuring the elasticity constants (μ_T, μ_L and E_T/E_L) needed to fully characterize an incompressible, TI tissue through dual-probe SWE. According to Equation 4.6, the shear moduli could be estimated with a single transducer through the velocity curve of PT propagation mode but it was difficult to measured both μ_T and μ_L with this method. In fact, as shown in Figure

5.3, only the velocities in a direction perpendicular to the beam could be estimated. Therefore, μ_T and μ_L were measured separately from shear wave propagation velocities with a single-probe set-up. Once calculated the shear moduli, E_T/E_L ratios were estimated through the WNLLS fitting of the data points obtained with dual-probe SWE. Figure 5.8 showed a good fitting for phantoms 2, 4 and 5 and confirms the possibility of using dual-probe set-up as a tool for estimating the mechanical properties of a TI phantom.

Among the articles on Shear Wave Elastography, we could not find any study on the dual-probe set-up hence it was not possible to compare the technique developed in this thesis with other works. Conventional SWE is still a new technique and, in my opinion, the research groups have been so far focused on optimizing the single-probe set-up in order to evaluate more in detail which kind of information could be obtained from it without trying to change the set-up. The studies based on conventional SWE always relate tissue stiffness with the shear modulus and try to find a correlation between a variation of the shear modulus and a potential disease. However, some pathological conditions can also be related to the elastic moduli (like for breast [40] and liver [41]) and it is possible that in these cases the shear moduli calculated with conventional SWE are not sufficient to detect a disease. Therefore, dual-probe SWE adds new information to conventional SWE and could detect diseases which are not detected with conventional SWE. Further investigations are needed to analyse a possible clinical applicability of dual-probe SWE.

6.5 Limitation

In the development of a transversely isotropic phantom, despite the procedure being the same for all the phantoms, the results did not show a constant ratio between the elastic moduli in the two main directions. The results could have been influenced by slight differences as thawing temperature, FT-cycles time or evaporation of water during the preparation of the solution. Moreover, with this kind of procedure a high level of anisotropy was difficult to reach for two main reasons: the maximum strain that could be applied during the stretching was limited by the risk of breaking the phantom; reducing the PVA density to increase the strain during the stretching decreased also the manoeuvrability for the mechanical tests. In order to overcome these limitations, it was important to write comments during the development of each phantom to understand unexpected results and add improvements to the following times.

During the mechanical tests, a limitation was introduced by the oblique surfaces of the samples and was reduced by a constant pre-compression before each test and a careful cutting during the preparation of the samples.

Both conventional and dual-probe SWE were limited by the angle between the phantom and the pushing beam. In the first case, the probe was placed perpendicularly to the table and the phantom was placed in a tank filled with water. If the phantom was isotropic this would not have been a problem but with a TI phantom, if it rotated, the probe did not collect the data from either the plane or the axis of isotropy but another plane which had different mechanical properties. Likewise, in the dual-probe set-up the angle between the probes and the table was 45 degrees (Figure 4.15(a)). This angle was difficult to reach with high precision and, as before, we might have collected the data from a different plane than the isotropy one. Before each dual-probe SWE test, B-mode images were collected with both the transducers in order to set their focal points approximately in the middle of the specimen. Moreover, during each test the transducers were clamped to a support to reduce the artefacts due to the their movement and to acquire data always from the same direction.

6.6 Future Outlook

Shear wave elastography has been commercially used with successful results for isotropic tissue. The attempts made to expand this technique into non-isotropic tissue have been limited by the difficulties in assessing a wave motion properly.

The presented work is a starting point for future studies on transversely isotropic tissue which is the simplest case of anisotropy.

A possible next step can be to define a repeatable procedure for developing a TI phantom trying to reach a constant value of E_T/E_L. Afterwards the procedure can be improved to mimic specific biological tissue, for example, by changing PVA density according to the density of the tissue, increasing or decreasing the number of FT-cycles to obtain the same tissue stiffness or varying the constant strain during the stretching to reach a specific ratio between the elastic moduli in the two main directions.

Moreover, the phantom developed in this study was made for large TI tissue neglecting guided waves. A further development could be studying this kind of waves in a TI tissue by developing a thinner phantom.

Dual-probe SWE represented the main novelty of this project and gave promising results in the phantom characterization. In the future, shear wave propagation velocities could be measured in more directions in order to obtain more data points to use for the WNLLS fitting. A reliable dual-probe SWE could also be used to measure the elastic parameters in transversely isotropic tissue even without knowing the direction of the fibers or without estimating the shear moduli from separate tests. The aim is to be able to measure all the three parameters needed to characterise this kind of tissue by a single test.

Chapter 7

Conclusions

The aim of the presented work was to develop a transversely isotropic phantom and evaluate the possibility of characterizing its mechanical behaviour using dual-probe Shear Wave Elastography.

The transverse isotropy of the developed phantoms was confirmed by both mechanical and SWE tests. First, mechanical tests showed a higher elastic modulus in the longitudinal direction than in the transverse direction. Second, conventional Shear Wave Elastography proved that the phantoms were homogeneous and the induced shear wave was travelling faster in the longitudinal direction than in the transverse direction. In general, the results obtained with both these procedures indicated a good agreement with what expected from the theory suggesting SWE as a valid tool to evaluate a TI tissue.

The main novelty of the project was the development of dual-probe SWE for a multiple mode characterization of induced shear wave. In particular, the goodness of the fitting between the theoretical curves of shear wave propagation and the data collected through this procedure represented not only a potential progress in research in the fully mechanical characterization of a TI tissue but also a possible tool for calculating the ratio between the elastic moduli in the transverse and longitudinal direction without mechanical tests.

Bibliography

[1] Axel Kaselow. The stress sensitivity approach: Theory and application. Master's thesis, Geburtsort: Düsseldorf, Deutschland, 2004.

[2] Peter Gudmundson. *Material Mechanics*. Department of Solid Mechanics, KTH Engineering Sciences, Stockholm, Sweden, 2006.

[3] Abigail Thrush Peter R. Hoskins, Kevin Martin. *Diagnostic Ultrasound: Physics and Equipment*. Cambridge University Press, New York, 2010.

[4] J.D. Landstreet. *Physical processes in the solar system: an introduction to the physics of asteroids, comets, moons and planets*. Keenan & Darlington Publishers, Canada, 1st ed. london edition, 2003.

[5] J. Brin Fowlkes Armen P. Sarvazyan, Oleg V. Rudenko. Scott D. Swanson and Stanislav Y. Emelianov. Shear wave elasticity imaging: a new ultrasonic technology of medical diagnostics. *Ultrasound in Medicine & Biology,*, pages 1419–1435, 1998.

[6] M. Tanter J. Bercoff and M. Fink. Supersonic shear imaging: A new technique for soft tissue elasticity mapping. *IEEE Transactions of ultrasonics, ferroelectrics, and frequency control*, 51(4):396–409, April 2004.

[7] Michael H. Wang. Shear wave imaging using acoustic radiation force. Master's thesis, Department of Biomedical Engineering, Duke University, 2013.

[8] Ron Daigle. *Sequence Programming Tutorial*. April 2012.

[9] Alireza Sadremomtaz Mahsa Noori Asl. Analytical image reconstruction methods in emission tomography. *J. Biomedical Science and Engineering*, 6:100–107, 2013.

[10] Mark L. Palmeri Kathy R. Nightingale Ned C. Rouze, Michael H. Wang. Finite element modeling of impulsive excitation and shear wave propagation in an incompressible, transversely isotropic medium. *Journal of Biomechanics*, September 2013.

[11] Tim Nordenfur. Comparison of pushing sequences for shear wave elastography. Master's thesis, KTH Technology and Health, Stockholm, 2013.

[12] Michael Insana James F. Greenleaf, Mostafa Fatemi. Selected methods for imaging elastic properties of biological tissues. *Annu. Rev. Biomed. Eng*, 2003.

[13] Martin H. Sadd. *Elasticity: Theory, Applications, and Numerics (2nd edition)*. Elsevier, 2009.

[14] Leslie R. Smith Horst Czichos, Tetsuya Saito. *Springer Handbook of Materials Measurement Methods*. Springer, 2006.

[15] Thomas Deffieux Daniel Royer, Jean-Luc Gennisson and Mickael Tanter. On the elasticity of transverse isotropic soft tissues. *The Journal of the Acoustical Society of America*, 129(5):2757–60, May 2011.

[16] Thomas L. Szabo. *Diagnostic Ultrasound Imaging: Inside Out(Second Edition)*, volume 41(2). Ultrasound in Medicine & Biology, Boston University, Boston, MA, USA, February 2015.

[17] Allan F. Bower. *Applied Mechanics of Solids*.

[18] David Larsson. Accuracy assessment of shear wave elastography for arterial applications by mechnical testing. Master's thesis, KTh, Royal Institute of Technology, Stockholm, 2014.

[19] M. M. Taverne and A. H. Willemse. Diagnostic ultrasound and animal reproduction. *Kluwer Academic Publishers*, 1989.

[20] Roger Nightingale Kathryn Nightingale, Mary Scott Soo and Gregg Trahey. Acoustic radiation force impulse imaging: in vivo dempstration of clinical feasibility. *Ultrasound in Medicine & Biology*, 28(2):227–235, 2001.

[21] K. Kirk Shung. *Diagnostic Ultrasound: Imaging and Blood Flow Measurements*. CRC Press, 2006.

[22] Tanter M. Quantitative assessment of breast lesion viscoelasticity: initial clinical results using supersonic shear imaging. *Ultrasound. Med. Biol.*, 34:1373–86, 2008.

[23] Berg W. Shear-wave elastography improves the specificity of breast us: the be1 multinational study of 939 masses. *Radiology*, 262(435-49), 2012.

[24] Tomy Varghese Luc Bidaut Ghulam Nabi Sarfraz Ahmad, Rui Cao. Transrectal quantitative shear wave elastography in the detection and characterisation of prostate cancer. *Surgical Endoscopy*, 27(9):3280–3287, 2013.

[25] Carmen C. M. Cho Edmund H. Y. Yuen Yolanda Y. P. Lee Anil T. Ahuja Kunwar S. S. Bhatia, Cina S. L. Tong. Shear wave elastography of thyroid nodules in routine clinical practice: preliminary observations and utility for detecting malignancy. *European Radiology*, 22(11):2397–2406, 2012.

[26] Bavu E et al. Noninvasive in vivo liver fibrosis evaluation using supersonic shear imaging: a clinical study on 113 hepatitis c virus patients. *Ultrason. Med. Biol.*, 37(1361-73), 2011.

[27] Dahl J J Frinkley K D Palmeri M L, Wang M H and Nightingale K R. Quantifying hepatic shear modulus in vivo using acoustic radiation force. *Ultrasound Med. Biol.*, 34(546–58), 2008.

[28] E. Macé G. Montaldo M. Fink J. L. Gennisson, T. Deffieux and M. Tanter. Viscoelastic and anisotropic mechanical properties of in vivo muscle tissue assessed by supersonic shear imaging. *Ultrasound Med. Biol.*, 36(5):789–801, 2010.

[29] Jean-Luc Gennisson Jeremy Bercoff M. Tanter, D. Touboul and Mathias Fink. High-resolution quantitative imaging of cornea elasticity using supersonic shear imaging. *IEEE transactions on medical imaging*, 28(12), 2009.

[30] J L Gennison J Brum, M Bernal and M Tanter. In vivo evaluation of the elastic anisotropy of the human achilles tendon using shear wave dispersion analysis. *Phys. Med. Biol.*, 59:505–523, 2014.

[31] C Prada E Messas J Emmerich P Bruneval A Citon M Fink M Couade, M Pernot and M Tanter. Quantitative assessment of arterial wall biomechanical properties using shear wave imaging. *Ultrasound in Med. Biol.*, 36(10):1662–1676, 2010.

[32] Ilya Tsvankin. *Seismic Signatures and Analysis of Reflection Data in Anisotropic Media.* Seismic Exploration 29. Pergammon, Amsterdam, 2001.

[33] Ned Rouze Kathryn Nightingale Michael Wang, Brett Bryamm Mark Palmieri. Imaging transverse isotropic properties of muscle by monitoring acoustic radiation force induced shear waves using a 2-d matrix ultrasound array. *IEEE transactions on medical imaging*, 32(9):1671–84, 2013.

[34] S. F. Levinson. Ultrasound propagation in anisotropic soft tissues: The application of linear elastic theory. *J. Biomech.*, 20(3):251–260, 1987.

[35] Nikolaos A. Peppas Christie M. Hassan. Structure and applications of poly(vinyl alcohol) hydrogels produced by conventional crosslinking or by freezing/thawing methods. *Springer-Verlang Berlin Heidelberg.*

[36] Thomas Deffieux Clément Papadacci Patrice Flaud Amir Nahas Claude Boccara Jean-Luc Gennisson Mickael Tanter Simon Chatelin, Miguel Bernal and Mathieu Pernot. Anisotropic polyvinyl alcohol hydrogel phantom for shear wave elastography in fibrous biological soft tissue: a multimodality characterization. *Physics in Medicine & Biology*, 59:6923–6940, 2014.

[37] Sinkus Ralph Geng Guangqiang Cheng Shaokoon Green Michael Rae Caroline D. Bilston-Lynne E. Qin, Eric C. Combining mr elastography and diffusion tensor imaging for the assessment of anisotropic mechanical properties: A phantom study. *Journal of Magnetic Resonance Imaging*, 37(1):217–226.

[38] Mohammadi H Millon L E and Wan W K. Anisotropic polyvinyl alcohol hydrogel for cardiovascular applications. *J. Biomed. Mater. Res. B Appl. Biomater*, 79:305–311, 2006.

[39] Bo Qiang Randall R Kinnick Ivan Z Nenadic James F Greenleaf Sara Aristizabal, Carolina Amador and Matthew W Urban. Shear wave vibrometry evaluation in transverse isotropic tissue mimicking phantoms and skeletal muscle. *Physics in Medicine and Biology*, 59:7735–7752, 2014.

[40] Judit Zubovits Abbas Samani and Donald Plewes. Elastic moduli of normal and pathological human breast tissues: an inversion-technique-based investigation of 169 samples. *Physics in Medicine and Biology*, 52(6), 2007.

[41] Yung-Ming Jeng Hey-Chi Hsu Po-Ling Kuo-Meng-Lin Lia Pei-Ming Yang Po Huang Lee Wen-Chun Yeha, Pai-Chi Li. Elastic modulus measurements of human liver and correlation with pathology. *Ultrasound in Medicine and Biology*, 28(4):467–474, 2002.

Appendix A

Matlab script for mechanical tests

Here is presented the code for the mechanical post-processing for the four tests in the plane of isotropy.

```
% import the data of the strain and the stress from the xls file.
% strain = n x 4 vector where each column correspond to the strain
% values of a single test
% stress = n x 4 vector where each column correspond to the stress
% values of a single test
% stretch = n x 4 vector where each column correspond to the stretch
% values of a single test

%% Linear Least Square LLS - Hooke law
for i=1:4
% Model
G=[strain(:,i)/100 ones(length(strain),1)];
p_est(:,i)= G\stress(:,i);
% Predicted stress
y_pred_L(:,i)=G*p_est(:,i);
E_L(i)=p_est(1,i);
end
E_LLS=coeff(1) % Average elastic modulus
SD_L=std(E_L) % standard deviation
```

```
%% Linear Least Square LLS - Neo Hookean
for i=1:4
% Model
G=[2*(stretch(:,i).^2-1./(stretch(:,i))) ones(length(stretch),1)];
p_est(:,i)= G\stress(:,i);
% Predicted stress
y_pred_NH(:,i)=G*p_est(:,i);
E_NH(i)=6*p_est(1,i);
end
E_LLS_NH=mean(E_NH) % Average elastic modulus
SD_NH=std(E_NH) % standard deviation
& Code for the plotting of the curve

%% Linear Least Square LLS - Mooney-Rivlin
for i=1:4
% Model
G=[2*(stretch(:,i).^2-1./(stretch(:,i))) -2*(1./(stretch(:,i).^2)+
   -stretch(:,i)) ones(length(stretch),1)];
p_est(:,i)= G\stress(:,i);
% Predicted stress
y_pred_MR(:,i)=G*p_est(:,i);
E_MR(i)=6*(p_est(1,i)+p_est(2,i));
end
E_LLS_MR=mean(E_MR) % Average elastic modulus
SD_MR=std(E_MR) % standard deviation
```